Universiteit Antwerpen

Faculteit Wetenschappen

Departement Fysica

Gilbert damping and noise in magnetic GMR multilayers

Proefschrift voorgelegd tot het behalen van de graad van
Master of Nanophysics
aan de Universiteit Antwerpen door

Martin Keller

Promotor: prof. dr. F. M. Peeters
Co-promotoren: dr. W. Van Roy (IMEC, Leuven)
dr. L. Lagae (IMEC, Leuven)

Antwerpen, 2007

Acknowledgements

It is that unique gift that some physics professors have to ignite and cultivate immense scientific enthusiasm, to a point of being able to change a students destiny.
I am mostly thankful to prof. dr. F. M. Peeters for first having motivated me to follow the nanophysics program and second for having made it possible to realize this thesis in collaboration with IMEC, Leuven. I remember my first contact two years ago, as I came from the industry and asked very elementary questions about GMR and spintronics.

In the same line as above, my great admiration and gratitude to prof. dr. B. Partoens. His guidance, lectures, remarkably personal dedication and the many interesting discussions on quantum mechanics have been of great help to me.

My special thanks to my co-promotors dr. W. Van Roy and dr. L. Lagae from IMEC. It has been a true privilege and pleasure for me having been initiated in the emerging field of spintronics at a research center as IMEC with an international reputation.
In my search for answers on GMR and spintronics I couldn't have found any better mentors.

I equally would like to thank all the academic staff of the physics department at the University of Antwerp who have contributed to the nanophysics program. I truly enjoyed every single lecture !

Beyond the scientific knowledge and expertise gained, more importantly to me are the many new personal acquaintances. These shall remain very precious to me.

To my beloved wife Dahlia, our children Rebecca and Glenn,

Martin Keller

Contents

List of abbreviations

DMS	Diluted Magnetic Semiconductors
EEPROM	Electrically Erasable Programmable Read Only Memory
FMR	Ferromagnetic Resonance
GMR	Giant Magneto Resistance
LLG	Landau-Lifshitz-Gilbert
MRAM	Magnetoresistive Random Access Memory
NIST	National Institute of Standards and Technology (USA)
OOMMF	Object Oriented Micromagnetic Framework
SMT-MRAM	Spin Momentum Transfer - Magnetic Random Access Memory
Spin FET	Spin Field Effect Transistor
Spin LED	Spin Light Emitting Diode
STO	Spin Torque Oscillator
TCL/TK	Tool Command Language/Tool Kit
WKB	Wentzel-Kramers-Brillouin

1

Introduction

1.1 SPIN BASED ELECTRONICS - SPINTRONICS

Since the invention of the transistor in 1947 by W. Shockley, J. Bardeen and W. Brattain conventional mainstream electronics has been based on charge transfer processes fully ignoring the spin of the electron. With recent progress in nanophysics and nanotechnology a new area has emerged called magneto-electronics or spintronics. In spintronics or spin based electronics it is not the electron charge but the electron spin that carries information. This offers opportunities for a new generation of devices combining traditional micro-electronics with spin-dependent effects that arise from the interaction between the spin of the carrier and the magnetic properties of the material. Adding the spin degree of freedom to conventional charge based electronics will add substantially more capabilities and performance to electronic products.

In traditional quantum physics the approach is to use the alignment of the electron spin as "spin up" or "spin down" relative to a reference eg. an applied magnetic field or orientation of a ferromagnetic film. In spin based devices, quantum spin interference effects will trigger device operations not only based on a quantity of electrical current but also based on a quantity of spin density or spin accumulation. Obviously spintronics requires a deep understanding of nanomagnetism and spin interactions in general.

Major challenges still exist in the field of spintronics and are addressed by experiments and theory. They mainly include a better understanding of the microscopic theory of spin quantum transport, optimization of electron spin lifetimes, spin coherence and spin polarized injection techniques. Im-

provements in characterization techniques and realization of stacked magnetic nanostructures have succeeded in matching theory and experiment.

The discovery of the Giant Magneto Resistance effect (GMR) by M.N Baibich and A. Fert 1988 is considered as the birth of spintronics. The GMR effect is the variance in resistivity of a magnetic structure consisting of magnetic and non magnetic materials under the application of an external magnetic field. GMR on its own has created, in less than 10 years, important technological applications such as GMR magnetic sensors used as read heads in all computer hard disks. GMR is a passive measurement of a change in resistivity under influence of an applied external magnetic field. A second important impulse to spintronics was the active injection of a spin polarized current into the magnetic multilayered structure. Most of today's publications in spintronics refer to the original paper of J.C. Slonczewski (IBM) from 1996 describing the spin transfer and spin torquing effects in multilayered magnetic film structures and predicting astonishing new fast, non volatile, switching phenomena. [1]. Again, in less then 10 years time, this had led to novel Magnetic Random Access Memories (MRAM) with far better read/write access time specifications and less wear out and lower power consumption than traditional Electrically Erasable Programmable Read Only Memory (EEPROMS).

In traditional electronics semiconductors are used as substrates and charge carriers. Today's emerging spintronics applications are based on magnetic metals. Future semiconductor spintronics will have two strands: magnetic doping of the semiconductors, Diluted Magnetic Semiconductor (DMS), or the use of spin-polarized currents in non-magnetic semiconductors. However it is generally believed that the first applications of semiconductor spintronics are still far out. DMS, if they can be made to operate at room temperature, could form a base for a complete spintronic overhaul of today's electronic components e.g. Spin Torque Oscillators (STO), spin Field Effect Transistors (spin FET), spin Light Emitting Diodes (spin LED), Spin Momentum Transfer Magnetoresistive Random Access Memory (SMT-MRAM) and other sensors.

1.2 GILBERT DAMPING AND NOISE IN MAGNETIC GMR MULTILAYERS

The field of magneto-electronics is based on two important discoveries: GMR and, very recently, spin transfer. GMR arises in ferromagnet-normal metal-ferromagnet (F/N/F) structures due to spin-dependent scattering of electrons. It can be seen as an interaction of the electrical current and the magnetic films. Spin transfer describes the interaction of the spin current and the dynamics of magnetic films. The spin current can be either a spin-polarized electrical current (e.g. after passing through a first ferromagnet), or a spin current without net electrical current (e.g. emitted by a precessing magnetization). The transferred spin angular momentum to the ferromagnet causes a torque

on the magnetization and may e.g. lead to magnetization reversal or drive an oscillation of the magnetization. Where GMR already finds its application in sensors or read heads, spin transfer and related effects are relatively new and their importance remains unexplored. They may lead to new applications such as memories based on current induced magnetic switching, but will also influence the characteristics and noise performance of GMR sensor devices, especially in the high frequency limit where the spin transfer effects influence the magnetic response of the system, e.g. as an enhancement of the Gilbert damping.

This thesis aims to get an insight in the role of spin transfer effects in GMR multilayer stacks typically used in sensor devices. Through simulation, we will reveal the importance of mutual spin transfer torques and enhanced damping in realistic spin valve sensors. Micromagnetic simulation as well as high frequency noise spectroscopy give direct information on the dynamical modes and damping in the device. These methods provide information on the importance of spin transfer and thermal fluctuations on high frequency noise. Such information is vital in understanding and controlling the limits of magnetic sensors, read heads and magnetic storage.

1.3 THESIS ORGANIZATION

In this thesis we study the main theoretical effects which are driving novel spintronic applications. In the second chapter we start from the basic Landau-Lifshitz-Gilbert equations (LLG) and derive the magnetic energy contributions that form the magnetic energy functional. Self consistent solving of the LLG equations with respect to the minimization of the magnetic energy functional leads to well known micro-magnetic simulations of hysteresis cycles of various magnetic materials.

In the third chapter we review the original paper of J.C. Slonczewski describing the spin transfer and spin torquing phenomena. The results described by J.C. Slonczewski have been obtained by using a formal scattering matrix approach, in our opinion far easier to understand than the original WKB method used in the original paper. In chapter four we analyze and simulate, first in a macro-spin model, the new phenomena emerging from the additional spin torquing term to the LLG equations. The macro-spin study will give us a good insight into the switching currents, time scales of the observed magnetization phenomena and the effects of external magnetic fields. We pay mainly attention to microwave oscillations and full magnetization reversal. Adding Langevin dynamics to obtain stochastic LLG equations is used to study the effect of temperature dependent switching. In the fifth chapter we expand the macro-spin results to the study of full magnetic domain motion adding the effect of demagnetizing fields. We simulate full MRAM dynamics and pay attention to coherent and non coherent noise effects during the high frequency magnetic precession.

In the sixth chapter we describe the theoretical effect of enhanced Gilbert damping which is linked to new phenomena called spin pumping.

In the last chapter we review the latest circuit theory of spin transfer torques in symmetric and asymmetric spin valves. These spin torque terms are currently most widely used in technological application.

The main simulation tools throughout this thesis are based on a public micromagnetic code developed by the US National Institute of Standards and Technology (NIST). This open software platform is called Object Oriented Micromagnetic Framework (OOMMF), [16].

During the realization of this thesis the latest version OOMMF 1.2.a.4 was released including various spin torquing terms allowing full simulation of magnetization reversal effects by injecting spin polarized currents into any chosen magnetic nano-structure.

1.4 GIANT MAGNETO RESISTANCE

Giant Magneto resistance is one of the most remarkable discoveries in thin film magnetic materials discovered in 1988 by M.N. Baibich and A. Fert. Within just a decade GMR sensors have been introduced in all hard-disk read-out units. We summary the main aspects of GMR as it is a fundamental pillar of all future spintronics developments. GMR is the change in electrical resistance in response to an applied magnetic field. It was discovered that the application of a magnetic field to a Fe/Cr multilayer resulted in a significant reduction of the resistance of the multilayer. This effect was found to be much larger than ordinary or anisotropic magnetoresistance and therefore was called Giant Magneto Resistance. High magnetoresistance can also be obtained in Co/Cu and Fe/Cr/Fe multilayers. In order to observe GMR one has to provide an opportunity to reorient the magnetic moments of the ferromagnetic layers relative to one other. In magnetic multilayered structures this can be achieved by the use of an antiferromagnetic interlayer coupling. By choosing an appropriate thickness of the non-magnetic layer it is therefore possible to create an antiparallel configuration of the ferromagnetic layers and then realign the moments by an applied external magnetic field.

1.4.1 Origin of GMR

The electrical conductivity of metals can be described by 2 large independent conducting channels corresponding to the up-spin and down spin- electrons, which are distinguished according to the projection of their spins according the quantization axis. The probability of spin scattering processes in metals is normally small as compared to the probability of the scattering processes in which the spin is conserved. This means that spin-up and spin-down electrons do not mix over long distances and therefore, the electrical conduction occurs

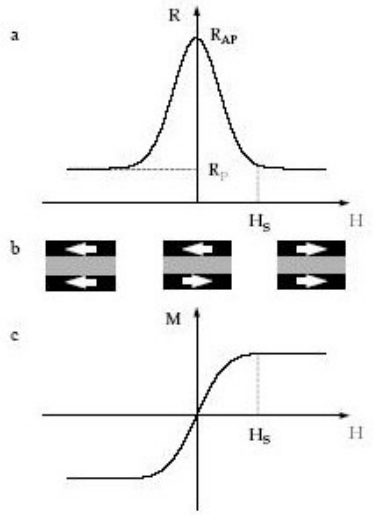

Fig. 1.1 Schematic representation of the GMR effect [8]. a) change of resistance of the magnetic multilayer as a function of applied magnetic field. b) The magnetization configuration of the magnetic multilayer as function of an external magnetic field. The magnetizations are aligned antiparallel at zero field; the magnetizations are aligned parallel when the external field H_{ext} is larger than the saturation field H_s. c) Magnetization curve for the multilayer.

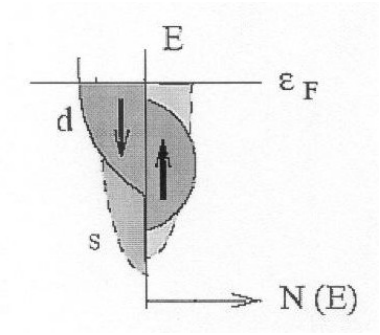

Fig. 1.2 Density of states spin up and spin down.

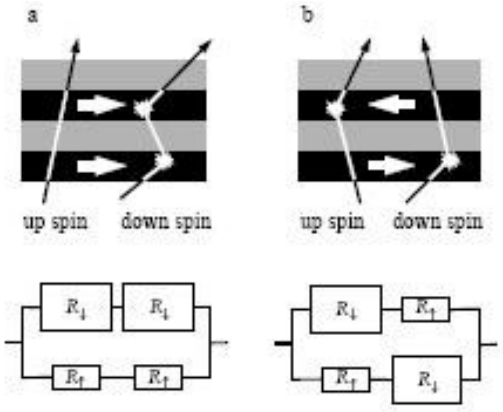

Fig. 1.3 Schematic illustration of electron transport in a multilayered magnetic material for parallel (a) and anti-parallel (b) magnetizations of successive layers. The electrical equivalent circuit illustrates the 2 different layer resistivities in function of their magnetization direction.

in parallel for the two spin channels. In ferromagnetic metals the scattering rates of the spin-up and spin-down electrons are quite different. The electric current is primarily carried by electrons from the sp bands due to their low effective mass and high mobility. The d bands play an important role in providing final states for the scattering of the sp electrons. In transition metal ferromagnets the d bands are exchange split, so that the density of states are different for the up and down-spin electrons at the Fermi level, see fig. (1.2). Using these arguments we can easily explain GMR in magnetic multilayers. We consider collinear magnetic configurations as shown in fig.(1.3). The difference in density of states for the up and down conduction channels, related

to the different resistivities by the Landauer-Büttiker relation, in function of a parallel or anti-parallel magnetization. This leads to a macroscopic equivalent electrical resistor model which works well in practice.

1.4.2 GMR equivalent resistor model

According to the resistor model each metallic layer (and each interface) is treated as an independent resistor. Within each spin conduction channel the resistors are added in parallel or in series depending on the relationship between the mean free path and the free layer thickness. In order to obtain a non zero GMR the mean free path should be sufficiently long. This is consistent with the qualitative picture of GMR which is based on the possibility for the electrons to propagate across the non-magnetic spacer freely, sensing the magnetizations of the two consecutive ferromagnetic layers. We denote the majority- and minority-spin resistivities of the ferromagnetic layer respectively equal $\rho_\uparrow$ and $\rho_\downarrow$. The resistance of the bilayer, which consists of the ferromagnetic layer and the spacer layer, for either of the two spin channels is equal to:

$$R_{\uparrow,\downarrow} = \rho_{NM} d_{NM} + \rho_{\uparrow,\downarrow} d_{FM} \tag{1.1}$$

where ρ_{NM} denote the resistivity and the thickness of the non-magnetic spacer layer t_{FM} is the thickness of the ferromagnetic layer. The total resistance of the parallel-aligned multilayer is then given by:

$$R_P = N \frac{R_\uparrow R_\downarrow}{R_\uparrow + R_\downarrow} \ . \tag{1.2}$$

The total resistance of the antiparallel-aligned multilayer is:

$$R_{AP} = N \frac{R_\uparrow + R_\downarrow}{2} \tag{1.3}$$

where N is the number of P or AP aligned layers. The GMR ratio is determined by the simple expression:

$$\frac{\Delta R}{R} = \frac{R_{AP} - R_P}{R_P} = \frac{(R_\downarrow - R_\uparrow)^2}{4 R_\downarrow R_\uparrow} \ . \tag{1.4}$$

Note that within this definition GMR is normalized to the low resistance and so GMR can be larger than 100 percent. Defining the spin asymmetry parameter $\alpha = \rho_\downarrow / \rho_\uparrow$ we obtain :

$$\frac{\Delta R}{R} = \frac{(\rho_\downarrow - \rho_\uparrow)^2}{4 \rho_\downarrow \rho_\uparrow} = \frac{(\alpha - 1)^2}{4\alpha} \ . \tag{1.5}$$

2

Generalized Landau-Lifshitz-Gilbert equations

2.1 GYROMAGNETIC PRECESSION

From quantum mechanics we know the proportionality between the magnetic moment μ and angular momentum L of electrons. This relationship can be expressed as :

$$\vec{\mu} = -\gamma_e \vec{L} \ , \tag{2.1}$$

where $\gamma_e = 1,75e10^{11} s^{-1} T^{-1}$ is the absolute value of the gyromagnetic ratio expressed in SI units:

$$\gamma_e = \frac{g|e|}{2m_e} \ , \tag{2.2}$$

$g = \simeq 2$ is the Landé - factor, $e = -1,6\ 10^{-19} C$ is the electron charge, $m_e = 9,1\ 10^{-31} kg$ the electron mass. By applying the momentum theorem one can relate the rate of change of the angular momentum to the torque exerted on the particle by the external magnetic field H:

$$\frac{d\vec{L}}{dt} = \mu_0 . \vec{\mu} \times \vec{H} \ . \tag{2.3}$$

with $\mu_0 = 4\pi.10^{-7}$ H/m.
By using Eq. (2.1) we end up with a model describing the precession of the spin of the magnetic moment around the field.

$$\frac{d\vec{\mu}}{dt} = -\mu_0 . \gamma_e \vec{\mu} \times \vec{H} \ . \tag{2.4}$$

The frequency of precession is the Larmor frequency:

$$f_L = \mu_0 . \frac{\gamma_e H}{2\pi} = \frac{\gamma H}{2\pi} \ , \tag{2.5}$$

with

$$\gamma = \mu_0 . \gamma_e = 2.21 \ 10^5 \ s^{-1} (A/m)^{-1} \ , \tag{2.6}$$

Eq. (2.4) can be written for each spin magnetic moment within the elementary volume V_r:

$$\frac{d\vec{\mu_j}}{dt} = -\gamma \vec{\mu_j} \times \vec{H} \ , \tag{2.7}$$

where we consider the magnetic field H to be spatially uniform. By taking the volume average of both sides of the latter equation, we obtain :

$$\frac{1}{V_r} \frac{d \sum_j \vec{\mu_j}}{dt} = -\gamma \frac{\sum_j \vec{\mu_j}}{V_r} \times \vec{H} \ , \tag{2.8}$$

and finally using the definition of magnetization vector field $\vec{M}$, we end up with the following gyromagnetic precession model:

$$\frac{\partial \vec{M}}{\partial t} = -\gamma \vec{M} \times \vec{H} \ . \tag{2.9}$$

We note that $\gamma_e M \mu_0$ has dimensions of frequency as M is in A/m.

2.2 THE LANDAU LIFSHITZ EQUATION

The first dynamical model for the precessional motion of the magnetization was proposed by Landau and Lifshitz in 1935. Basically, this model is constituted by a continuum precession equation as in Eq. (**??**) in which the presence of all quantum mechanical effects and anisotropy is phenomenologically taken into account by means of an effective field H_{eff}. Then the Landau-Lifshitz equation is given by :

$$\frac{\partial \vec{M}}{\partial t} = -\gamma \vec{M} \times \vec{H_{eff}} \ . \tag{2.10}$$

We observe that the equilibrium condition is obtained for $\frac{\partial \vec{M}}{\partial t} = 0$. However, dissipative processes take place within the dynamic magnetization processes. The microscopic nature of this dissipation is still not clear and is today still the focus of considerable research.

The approach followed by Landau and Lifshitz consists in introducing dissipation in a phenomenological way. Gilbert proposed in 1955 a kind of viscous force, whose components are proportional to the time derivative of the magnetization. More specifically, Gilbert introduces the following additional torque term:

$$\frac{\alpha}{M_s} \vec{M} \times \frac{\partial \vec{M}}{\partial t} \ . \tag{2.11}$$

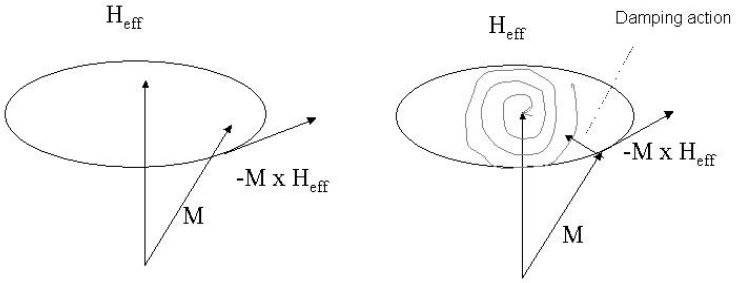

Fig. 2.1 (Left) Undamped gyromagnetic precession. (Right) Damped gyromagnetic precession.

Herein α is a dimensionless damping constant. Typically α has a value between 0,1 and 0,001. In fact the additional torque term is introduced to push the magnetization in the direction of the effective field, fig.(2.1). Then the Landau-Lifshitz equation becomes:

$$\frac{\partial \vec{M}}{\partial t} = -\gamma \vec{M} \times \vec{H_{eff}} + \frac{\alpha}{M_s} \cdot (\vec{M} \times \frac{\partial \vec{M}}{\partial t}) \ . \tag{2.12}$$

We also define a normalized magnetization $\vec{m} = \vec{M}/M_s$. This leads to the reduced LLG equation:

$$\frac{\partial \vec{m}}{\partial t} = -\gamma \vec{m} \times \vec{H_{eff}} + \alpha \cdot (\vec{m} \times \frac{\partial \vec{m}}{\partial t}) \ . \tag{2.13}$$

2.3 THE MAGNETIC STATE OF A BODY

When an external field H_{ext} is applied to a body, it will induce a magnetization density M. The magnetization density gives rise to magnetic charge density $\rho_m(r)$, which in turn gives rise to an induced demagnetizing field H_d. This changes the total field B, which changes the induced magnetizing field density, and so on... The magnetic state of a body has to be found by self-consistently finding the magnetization in the presence of the external field H such that the total energy is minimized.

2.3.1 The micromagnetic energy functional

To understand the magnetic state of a ferromagnet, we turn to a micromagnetic description. Micromagnetics are based on the same variational principles as used in thermodynamic principles. If we consider $m_\alpha, \alpha = x, y, z$ as the Cartesian components of a unit vector along the local magnetization direction and normalized against the saturation magnetization M_s, we are looking for an absolute or relative minimum under the constraint $m^2 = 1$. In this principle we ignore the rare cases in which this constraint is not valid eg. if the saturation magnetization is not constant inside a micromagnetic configuration. Another consequence of the minimum energy principle is that the torque on the magnetization has to vanish in each point. The full magnetic relaxation dynamics will be expressed when solving the Landau-Lifshitz-Gilbert equations.

In our micromagnetic model we include all relevant energy contributions on scales larger than some 10 nm. This means that as a rule of thumb, in actual numerical simulations, our grid size used should be less than 10 nm. In the next subsections we discuss the individual energy contributions and the internal micromagnetic energy competition [18],[19] and [14].

2.3.2 Exchange energy

Electron spin magnetic moments interact with each other through exchange coupling. As a consequence of the Pauli exclusion principle 2 electrons cannot occupy the same quantum state at the same place and time eg. same spin up or spin down states. Therefore, two electrons with the same spin orientation, through the Pauli exclusion principle, will lower their electrostatic (Coulomb) interaction energy by increasing their distance . Hence, the Pauli exclusion principle makes the total energy of the 2 parallel spins lower than that of two electrons with anti-parallel spins. The amount by which the Coulomb energy is reduced is called exchange energy and denoted by J. The Heisenberg exchange Hamiltonian for a cubic lattice is given by :

$$E_{ex} = -2J \sum_{i,j} \vec{S_i}.\vec{S_j} \ , \tag{2.14}$$

where the sum is restricted to the nearest neighbors only and $\vec{S_i}, \vec{S_j}$ are the spin angular momenta, expressed in units of $\hbar$, and J is the nearest neighbor exchange integral. Thus if $\vec{m_i}$ is the unit magnetization vector in the direction $-\vec{S_i}$, such that $\vec{S_i} = -S\vec{m_i}$ (S is the spin magnitude), and if $\theta_{i,j}$ is the small angle between the direction $\vec{m_i}$ and $\vec{m_j}$, we can rewrite Eq. (2.15) using a Taylor expansion:

$$E_{ex} = -2JS^2 \sum_{i,j} cos\theta_{i,j} \simeq -2JS^2 \sum_{i,j} (1 - \frac{1}{2}\theta_{i,j}^2) \tag{2.15}$$

$$E_{ex} = const. + JS^2 \sum_{i,j} \theta_{i,j}^2 \simeq const. + JS^2(\vec{m_j} - \vec{m_i})^2 \ , \tag{2.16}$$

since for small $\theta_{i,j}$, $|\theta_{i,j}| = |\vec{m_j} - \vec{m_i}|$. We assume that the displacement vector $\vec{m_j} - \vec{m_i}$ can be written in terms of a continuous function of m :

$$\vec{m_j} - \vec{m_i} = \Delta\vec{r_j}.\nabla\vec{m} \ , \tag{2.17}$$

where $\Delta\vec{r_j} = \vec{r_j} - \vec{r_i}$ is the position vector of neighbor j with respect to site i. With $\vec{m} = m_x\vec{1_x} + m_y\vec{1_y} + m_z\vec{1_z}$ we obtain,

$$E_{ex} = const. + JS^2 \sum_j (\Delta\vec{r_j}.\nabla\vec{m})^2 \ , \tag{2.18}$$

$$E_{ex} = const. + JS^2 \sum_j [(\Delta\vec{r_j}.\nabla m_x)^2 + (\Delta\vec{r_j}.\nabla m_y)^2 + (\Delta\vec{r_j}.\nabla m_z)^2] \ . \tag{2.19}$$

Summing over index j and multiplying over the total number of spins n per unit volume, we obtain the exchange energy ϵ_{ex} per unit volume. With $\Delta\vec{r_j} = x_j\vec{1_x} + y_j\vec{1_y} + z_j\vec{1_z}$, due to the cubic symmetry we have $\sum_j x_j y_j = 0$, and $\sum_j x_j^2 = 1/3 \sum_j \Delta r_j^2$. Using these properties and redefining the zero energy to absorb the constant term we obtain:

$$\epsilon_{ex} = A.[(\nabla m_x)^2 + (\nabla m_y)^2 + (\nabla m_z)^2] \ , \tag{2.20}$$

with A the exchange constant:

$$A = \frac{1}{6} nJS^2 \sum_j \nabla r_j^2 \ . \tag{2.21}$$

The exchange constant A in J/m can be easily adapted for the respective SC, BCC or FCC lattices. Typical values for A are 10^{-12} J/m, eg. NiFe 13.10^{-12} J/m. Finally we can write for the whole magnetic body:

$$E_{ex} = \int_V A[(\nabla m_x)^2 + (\nabla m_y)^2 + (\nabla m_z)^2]dV = A \int_V (\nabla\vec{m})^2 dV \ . \tag{2.22}$$

Applying the gradient operator twice on the identity $m^2 = 1$, we find another equivalent form:

$$E_{ex} = -A \int_V \vec{m}.\Delta\vec{m} \ dV \ , \tag{2.23}$$

with Δ=div grad being the Laplace operator. Numerically the exchange energy contribution from cell i is now given by [16]:

$$\epsilon_{ex,i} = \sum_{j \epsilon N_i} A \frac{\vec{m_i}.(\vec{m_i} - \vec{m_j})}{\Delta_{ij}^2} \ , \tag{2.24}$$

where N_i is the set consisting of the 6 cells nearest to cell i, A is the exchange coefficient in J/m, and Δ_{ij} is the discretization step size between cell i and cell j in meters. The exchange energy tries to keep the direction of the magnetization density as constant as possible.

2.3.3 Zeeman energy

The Zeeman energy term is due to the interaction of the magnetization density with an external magnetic field H_{ext}. The Zeeman interaction energy is simply:

$$E_z = -\mu_0.M_s \int_V \vec{H}_{ext}.\vec{m}\ dV\ . \tag{2.25}$$

For a uniform external field this energy depends only on the average magnetization and not on a particular magnetic domain structure. The Zeeman energy tries to align the magnetization direction with the external field.

2.3.4 Magnetostatic interactions

This energy contribution is connected to the magnetic field generated by the magnetic body itself. From Maxwell equations we can derive a magnetic pole density, or magnetic charge density, $\rho_m(r)$, as source of a magnetic field due to magnetization density M:

$$\nabla\vec{H}_d = -\nabla\vec{M} = \rho_m(r)\ . \tag{2.26}$$

The sinks and sources of these magnetic poles act like positive and negative "magnetic charges" creating magnetostatic interactions. The fields can be calculated in analogy with fields in electrostatics from electrical charges. The only difference is that magnetic charges never appear isolated but are always balanced by opposite charges. The magnetostatic interactions (energies trying to create a demagnetizing field) are long range effects within the magnetic domain. The effect of surface and volume charges will affect the magnetic state over a large distance. The magnetostatic interactions will tend to 'demagnetize' or 'degauss' the magnetic domain and therefore are also called the demagnetizing or degaussing energy. The demagnetizing energy is given by:

$$E_d = \frac{1}{2}\mu_0 \int_V H_d^2\ dV = \frac{1}{2}\mu_0.M_s \int_V \vec{H}_d.\vec{m}\ dV\ . \tag{2.27}$$

With $\rho_m(\vec{r}) = -\nabla\vec{M}$ for the volume charge density and $\sigma_m(r) = \vec{M}.\vec{n}$ being the surface charge density with outward pointing normal vector $\vec{n}$. With these quantities we obtain the potential of the degaussing field at position r by integration over r':

$$\phi_d = \frac{1}{4\pi\mu_0}[\int_V \frac{\rho_m(\vec{r}')}{|\vec{r}-\vec{r}'|}\ dV' + \int_S \frac{\sigma_S(\vec{r}')}{|\vec{r}-\vec{r}'|}\ dS'] \ . \tag{2.28}$$

From this equation we derive $\vec{H}_d(\vec{r}) = -\nabla\phi_d(\vec{r})$:

$$\vec{H}_d(\vec{r}) = -\int_V dV \frac{\nabla.\vec{M}(\vec{r})(\vec{r}-\vec{r'})}{|\vec{r}-\vec{r'}|^3} + \int_S \frac{\vec{n}(r').\vec{M}(\vec{r'})(\vec{r}-\vec{r'})}{|\vec{r}-\vec{r'}|^3}\ . \tag{2.29}$$

Magnetostatic self-interactions try to minimize the demagnetizing field energy by typically aligning the magnetization density parallel to the bounding surfaces. In micromagnetic macro-spin simulations, where only homogenous magnetization is being considered, the degaussing term is obviously being neglected.

2.3.5 Anisotropy energy

In ferromagnetic materials there is very often a preferred axis or plane of magnetization which is due to a particular symmetry in the crystal lattice. This effect is mainly explained due to differences in the interactions between the spin magnetic moments and the orbit magnetic moments along several crystal axes. In most experiments it is generally observed that in the absence of an external magnetic field, the ferromagnetic material is magnetized along precise directions, called easy directions. We can express this as a 'force' which tends to align the magnetization along the easy directions. This can be taken into account in our free energy functional as an additional phenomenological term. Our magnetization unit vector $\vec{m} = m_x\vec{1_x} + m_y\vec{1_y} + +m_z\vec{1_z}$ can be expressed in spherical coordinates as :

$$\begin{cases} m_x &= sin\theta cos\theta \\ m_y &= sin\theta sin\phi \\ m_z &= cos\theta \ . \end{cases}$$

The anisotropy energy density $f_{ani}(m)$ can be seen as a function of the spherical angles θ and ϕ, and the anisotropy energy as :

$$E_{ani}(\vec{m}) = \int_V f_{an}(\vec{m})dV \ . \tag{2.30}$$

In this phenomenological term, the easy directions are expressed as minima of the anisotropy energy density as a function of the angles θ and ϕ. As an example we treat one of the most frequent anisotropy effect being the uniaxial anisotropy. In this case the anisotropy free energy density $\epsilon_{ani}(\vec{m})$ will be rotationally symmetric with respect to an easy axis and will depend only on the relative orientation of m with respect to this axis. In the case of an easy direction along the z-axis, we can express $\epsilon_{ani}(m)$ as an even function of $m_z = cos\theta$. Using Eq. (2.28) we write $m_x^2 + m_y^2 = 1 - m_z^2 = sin\theta$, which we expand as:

$$\epsilon_{ani}(\vec{m}) = K_0 + K_1 sin^2\theta + K_2 sin^4\theta + K_3 sin^6\theta + ... \tag{2.31}$$

K_1,K_2 and K_3 are the anisotropy constants expressed in J/m^3. Usually, in the literature the expansion is truncated after the first term :

$$\epsilon_{ani}(\vec{m}) = K_0 + K_1 sin^2\theta \ . \tag{2.32}$$

In Eq. (2.32)we distinguish 2 cases. If $K_1 > 0$, the anisotropy energy has 2 minima, $\theta = 0$ and $\theta = \pi$, which expresses that the magnetization direction lies along the positive or negative z direction with no preferential orientation. This is called the easy axis anisotropy. In the case $K_1 < 0$, the energy is minimized for $\theta = \pi/2$, meaning that any direction in the x-y plane corresponds to an easy direction, called easy plane anisotropy. As an example we cite Cobalt with its hexagonal crystal structure and uniaxial anisotropy. As cubic crystal structure we have Fe, easy axis along (100)direction and $K_1 > 0$ and Ni, easy plane along (111) and $K_1 < 0$.

2.4 MICROMAGNETIC SIMULATIONS

We summarize the free micromagnetic energy functional consisting out of 4 energy contributions as derived in the previous section:

1. E_{ex} = Exchange energy due to spin/spin interactions on atomic scale level. Short range interactions.
2. E_z = Zeeman field energy as a result of the external field.
3. E_d = Degaussing energy or self magnetostatic energy. Long range domain wall interactions.
4. E_{ani} = Anisotropic energy due to spin/orbit interactions in the crystal lattice.

The free energy functional is given by:

$$E[\vec{m}(\vec{r})] = E_{ex}[\vec{m}(\vec{r})] + E_z[\vec{m}(\vec{r})] + E_d[\vec{m}(\vec{r})] + E_{ani}[\vec{m}(\vec{r})] \ . \tag{2.33}$$

with:

$$\begin{aligned}
E_{ex}[\vec{m}(\vec{r})] &= -A \int_V \vec{m}(\vec{r}).\Delta\vec{m}(\vec{r}) \ dV \\
E_z[\vec{m}(\vec{r})] &= -\mu_0.M_s \int \vec{m}(\vec{r}).\vec{H}_{ext}(\vec{r})dV \\
E_d[\vec{m}(\vec{r})] &\simeq -\frac{1}{2}\mu_0.M_s \int \vec{m}(\vec{r}).\vec{H}_d(\vec{r})dV \\
and \ \ \vec{H}_d(\vec{r}) &= -\int_V dV \frac{\nabla.\vec{M}(\vec{r})(\vec{r}-\vec{r'})}{|\vec{r}-\vec{r'}|^3} + \int_S \frac{\hat{n}(r').\vec{M}(\vec{r'})(\vec{r}-\vec{r'})}{|\vec{r}-\vec{r'}|^3} \\
E_{ani}[\vec{m}(\vec{r})] &= \ Depends \ on \ the \ specific \ form \ of \ anisotropy \ .
\end{aligned}$$

The different energetic terms are competing each other within cells of the full magnetic domain. Indeed, non collinear spins are increasing the exchange energy. The anisotropy energy will increase as the magnetization direction is deviating from the easy axis direction. The degaussing energy is also

influenced as magnetic poles change within the magnetic body. Similar to thermodynamic principles we use a variational technique to minimize the full micromagnetic energy functional with respect to $\vec{m}$. Calculating the functional derivative, taking into account the constraint $m^2 = 1$, we obtain after some cumbersome algebra:

$$\frac{\partial E[(\vec{m}(\vec{r})]}{\partial \vec{m}} = \vec{m}(\vec{r}) \times (A\nabla^2 \vec{m}(\vec{r}) + M_s \vec{H}_{ext}(\vec{r}) + M_s \vec{H}_d(\vec{r}) - \frac{\partial \epsilon_{ani}}{\partial \vec{m}(\vec{r})}) = 0 \ . \tag{2.34}$$

This expression simply states that the minimum energy state is such that the torque exerted locally by the local effective field on the magnetization is zero. The equilibrium magnetization is parallel to the local effective field $\vec{H}_{eff}$ given by:

$$\vec{H}_{eff}(\vec{r}) = \frac{A}{M_s}\nabla^2 \vec{m}(\vec{r}) + \vec{H}_{ext}(\vec{r}) + \vec{H}_d(\vec{r}) - \frac{\partial \epsilon_{ani}}{\mu_0 . M_s \partial \vec{m}(\vec{r})} \ . \tag{2.35}$$

Whatever numerical technique is used to solve the equations to find the minimum energy for magnetization, we will only find a local minimum. With different initial states, we may reach a different magnetization equilibrium. In the OOMMF code [16], following equations are being solved self consistently:

$$\frac{\partial E[\vec{M}(\vec{r})]}{\partial \vec{M}(\vec{r})} = \vec{m}(\vec{r}) \times \vec{H}_{eff}(\vec{r}) \ , \tag{2.36}$$

$$\frac{\partial \vec{M}(\vec{r})}{\partial t} = -\gamma \vec{M}(\vec{r}) \times \vec{H}_{eff}(\vec{r}) + \frac{\alpha}{M_s}(\vec{M}(\vec{r}) \times \frac{\partial \vec{M}(\vec{r})}{\partial t}) \ . \tag{2.37}$$

Scalar multiplication of Eq.(2.35) by $\vec{m}$ results in $\frac{1}{2}(\frac{d\vec{m}}{dt}) = 0$, which means the magnetization vector $\vec{m}$ is moving over the unit sphere. In practice, within OOMMF a random magnetization direction is used for each individual cell over the domain. H_{eff} is being calculated and used in the LLG equation to torque the magnetization vector towards H_{eff}. After each time step a new H_{eff} is calculated over the entire domain. A new magnetization vector results and further being torqued towards H_{eff} until convergence is obtained and the magnetization vector is aligned with H_{eff}. It means that the spatial orientation of the magnetization over the entire domain is given by minimization of the micromagnetic energy function. The time motion precessional dynamics are driven by the LLG equations. The most difficult term to calculate is the degaussing term. This is done numerically by taking the Fourier transform and using FFT's and IFFT's over the full domain. It is interesting to notice that such micromagnetic simulations are used to calculate and predict hysteresis loops and are used to study domain wall motions in general. Very often macrospin simulations are being carried out to provide good insight in the magnetization dynamics. In macrospin simulations the degaussing term is turned off and only homogenous magnetization is being considered, $\vec{m}(\vec{r}) = m$.

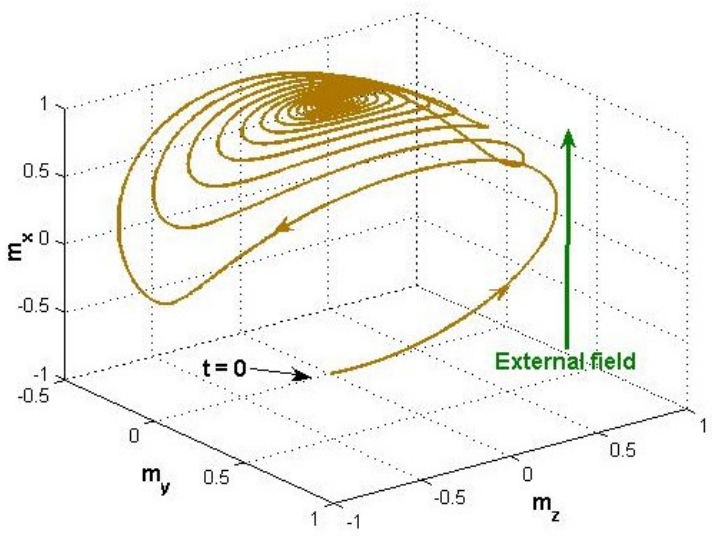

Fig. 2.2 Macrospin magnetization dynamics, over the unit sphere, with external magnetic field of 100 mT and Gilbert damping = 0,3. At t=0, normalized magnetization $m_x = -1$. Sampling time = 1 ps.

As an example we show in fig. (2.2) typical macrospin magnetization dynamics under the influence of an arbitrary external field and a Gilbert damping factor of 0,3.

2.4.1 Some computational aspects and the OOMMF numerical solver

In his subsection we mainly describe the numerical techniques used in OOMMF [16]. The micromagnetic problem is solved upon a regular 2D grid of squares, with 3D magnetization spins positioned at the centers of the cells. The constraint that the grid is composed of square elements takes priority over the requested size of the grid. The anisotropy and applied field energy terms are calculated using a closest neighbor interpolation technique, see Eq. (2.23). The degaussing field is calculated as the convolution of the magnetization against a kernel that describes the cell to cell magnetostatic interactions. The convolution is evaluated using Fourier transform (FFT) techniques. The LLG differential equation is integrated using a second order predictor integrator technique. The right side of Eq. (2.36), at the current and previous step is extrapolated forward in a linear fashion and is integrated across the new time interval to obtain a quadratic prediction for M at the next time step. At each stage the spins are renormalized to M_s. Failing to do so would create numerical instability. The right side of Eq. (2.36) is evaluated at the predicted M,

which is then combined with the value at the current step to produce a linear interpolation of $\frac{d\vec{M}}{dt}$ across the new interval. This is then integrated to obtain the final estimate of M at the new step. The local (one step) error of this procedure should be $O(\delta t^3)$. The step is accepted if the total energy of the system decreases, and the maximum error between the predicted and final M is smaller than a nominal value. If the step is rejected, then the step size is reduced and the integration procedure is repeated. If the step is accepted, then the error between the predicted and final M is used to adjust the size of the next step. No fixed ratio between the previous and current time step is assumed. A fourth order Runga-Kutta solver is used to drive the predictor-corrector solver. For a given applied field, the integration continues until an elapsed simulation time is reached or eg. $|\vec{M} \times \vec{H_{eff}}|/M_s^2$ drops below a given value implying an equilibrium state has been reached.

3

Slonczewski original sine spin torque term

In this chapter we calculate the current induced torques in metallic magnetic multilayers derived from transmission and reflection properties of the magnetic layers. J. Slonczewski [1] first formulated an additional spin transfer torque term in 1996. He predicted that a transfer of vectorial spin accompanies an electric current flowing perpendicular to two parallel magnetic films connected by a normal metallic layer. In his paper he used a WKB parabolic-band approximation, although only the end results are presented without any in depth calculations. Here we reproduce these results using a simplified scattering matrix method [11]. We pay attention to the phase averaging procedures and derivation of the angle dependent spin torque amplitude term as described by Slonczewski.
We also demonstrate a simple intuitive picture of the physics behind the spin transfer effect. In the next chapter we discuss in depth the consequences of the additional spin transfer torque term to the LLG equations resulting in new mesoscopic precession and switching phenomena.

3.1 DOUBLE BARRIER MAGNETIC STRUCTURE - SCATTERING MATRIX METHOD

We consider the sandwich structure ferromagnet/insulator/ferromagnet (FM1/NM/FM2) as depicted in fig.(3.1). We consider the 5 metallic regions where I,II and III are paramagnetic and FM1 and FM2 are ferromagnetic. The instantaneous vectors $\hbar S_1$ and $\hbar S_2$ forming the included angle θ represent the respective total spin momenta per unit area of the ferromagnets. We

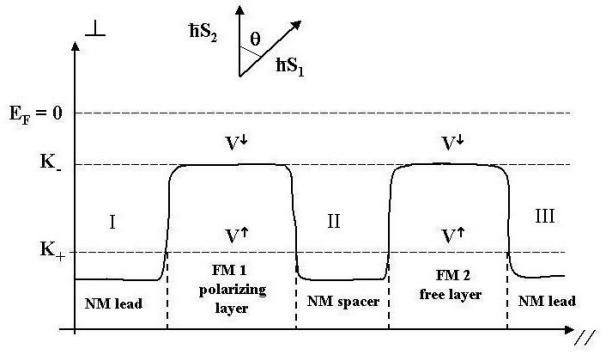

Fig. 3.1 Stoner band splitting and potentials $V^{\downarrow}, V^{\uparrow}$ representing minimum energy levels $(-)E_{\perp}$ for respective spin down and spin up electrons to freely tunnel trough the magnets.

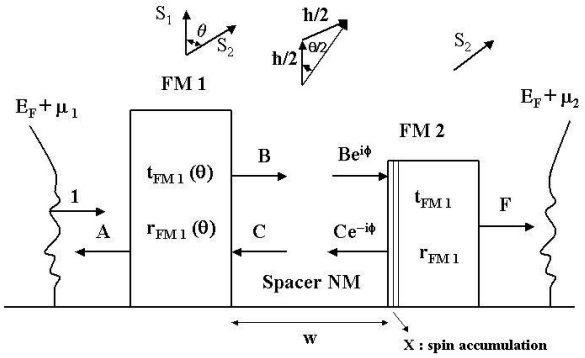

Fig. 3.2 Spin dependent double magnetic barrier structure including first fixed layer polarizing magnet FM1 and free layer magnet FM2. Spacer NM of width $W < 100\,nm$, sufficient thin to maintain spin coherency during tunneling in the ballistic assumption.

consider a flow of electrons moving through the sandwich from the left to the right. The assumption is that the thickness w of the spacer NM is less than the spin diffusion length, usually at least 100 nm. We now model our FM1/NM/FM2 structure as a double magnetic barrier structure and study the spin dependent tunneling considering the Stoner band splitting and accordingly the potentials for minority and majority carriers, $V^{\downarrow}$ and $V^{\uparrow}$ for the ferromagnets, see fig.(3.2). As suggested by Slonczewski we consider 3 classes of electrical current i_e and spin current I_s that can propagate through

our structure. Class "a" are electrons that have sufficient energy to fully transmit through the system, independently of spin up/down polarization. For an incident particle flux J_a of class "a" this contributes to an amount of $i_{ea} = eJ_a \neq 0$ and $I_{sa} = 0$ For class "c" we consider that all incident electrons are fully reflected, giving $i_{ec} = 0$ and $I_{sc} = 0$. Remains class "b" for which we make the assumptions that only the spin up electrons will fully transmit and spin down electrons will fully be reflected at each interface in the system. We calculate the class "b" transmission coefficient of the double barrier assuming that only spin up electrons will propagate throughout the full structure. We assign unity amplitudes to the incoming spinor wavefunctions $\psi_{in}^{\sigma\sigma}$ from the left, with σ being the spin state, and can write:

$$\begin{pmatrix} \psi_{in}^{\uparrow\uparrow} & \psi_{in}^{\uparrow\downarrow} \\ \psi_{in}^{\downarrow\uparrow} & \psi_{in}^{\downarrow\downarrow} \end{pmatrix} = \begin{pmatrix} 1 & 0 \\ 0 & 1 \end{pmatrix} = I \ .$$

For the reflection and transmission matrices of the ferromagnets we have respectively:

$$r_{FM1} = \begin{pmatrix} 0 & 0 \\ 0 & 1 \end{pmatrix} \ , \ t_{FM1} = \begin{pmatrix} 1 & 0 \\ 0 & 0 \end{pmatrix} \ , \ r_{FM2} = \begin{pmatrix} 0 & 0 \\ 0 & 1 \end{pmatrix} \ , \ t_{FM2} = \begin{pmatrix} 1 & 0 \\ 0 & 0 \end{pmatrix} \ .$$

We have to consider that an electron with initial spin state along the direction S_1 from FM1 is incident from region B onto FM 2. FM1 is the polarizing magnet. As the spin quantization reference frame of FM2 is rotated by a angle θ versus the quantization frame of FM1, we have to apply a rotation from the frame FM1 to the reference frame FM2. The rotation matrix $G(\theta)$ can be derived from figure (3.2). The $(\theta/2)$ is derived from the linear superposition of the initial spin states as the electron impinges from FM1 to FM2. We obtain :

$$G(\theta) = \begin{pmatrix} cos(\theta/2) & -sin(\theta/2) \\ sin(\theta/2) & cos(\theta/2 \end{pmatrix} \ .$$

Our scattering matrices r_{FM1} and t_{FM1} now transform into:

$$r_{FM1}(\theta) = G(\theta) \cdot \begin{pmatrix} 0 & 0 \\ 0 & 1 \end{pmatrix} \cdot G^{-1}(\theta) = \begin{pmatrix} sin^2(\theta/2) & -\frac{sin\ \theta}{2} \\ -\frac{sin\ \theta}{2} & cos^2(\theta/2) \end{pmatrix}$$

and

$$t_{FM1}(\theta) = G(\theta) \cdot \begin{pmatrix} 1 & 0 \\ 0 & 0 \end{pmatrix} \cdot G^{-1}(\theta) = \begin{pmatrix} cos^2(\theta/2) & \frac{sin\ \theta}{2} \\ \frac{sin\ \theta}{2} & sin^2(\theta/2) \end{pmatrix} \ .$$

As done by Slonczewski, we consider the most simple case with full transmission of $\psi^{\uparrow\uparrow}$ and full reflection of $\psi^{\downarrow\downarrow}$. Further we do neglect spin-flip scattering at the interfaces which results in the zero off-diagonal terms. We can write the reflection/transmission equations in matrix notation for the double

barrier structure with A,B,C and F as defined in fig. (3.2):

$$\begin{cases} A & = & r_{FM1}(\theta).I + t_{FM1}(\theta).C \\ B & = & t_{FM1}(\theta).I + r_{FM1}(\theta).C \\ C.e^{-i\phi} & = & r_{FM2}.B.e^{+i\phi} \\ F & = & B.t_{FM2}.e^{i\phi} \ . \end{cases}$$

Solving for B with $Z = e^{2i\phi}$ we obtain :

$$B = \sqrt{Z}[I - Zr_{FM1}(\theta)r_{FM2}]^{-1}t_{FM1}(\theta)$$

and

$$F = \sqrt{Z}\ t_{FM2}[I - Zr_{FM1}(\theta)r_{FM2}]^{-1}t_{FM1}(\theta)$$

resulting in:

$$\begin{pmatrix} B^{\uparrow\uparrow} & B^{\uparrow\downarrow} \\ B^{\downarrow\uparrow} & B^{\downarrow\downarrow} \end{pmatrix} = \sqrt{Z} \begin{pmatrix} \frac{-cos\ \theta+Z+Zcos\ \theta-1}{-2+Z+Zcos\ \theta} & \frac{-sin\ \theta+Zsin\ \theta}{-2+Z+Zcos\ \theta} \\ \frac{-sin\ \theta}{-2+Z+Zcos\ \theta} & \frac{-1+cos\ \theta}{-2+Z+Zcos\ \theta} \end{pmatrix}$$

$$\begin{pmatrix} F^{\uparrow\uparrow} & F^{\uparrow\downarrow} \\ F^{\downarrow\uparrow} & F^{\downarrow\downarrow} \end{pmatrix} = \sqrt{Z} \begin{pmatrix} \frac{2(Z-1)\sqrt{Z}cos^2(\theta/2)}{-2+Z+Zcos\ \theta} & \frac{(Z-1)\sqrt{Z}sin\ \theta}{-2+Z+Zcos\ \theta} \\ 0 & 0 \end{pmatrix} .$$

We calculate the particle transmission coefficient T as follows:

$$T = |F^{\uparrow\uparrow}|^2 + |F^{\uparrow\downarrow}|^2 = \frac{(Z-1)(1-Z)cos^2(\theta/2)}{Z\ |Zcos^2(\theta/2) - 1|^2} \ . \tag{3.1}$$

The spin density current I_s at point B can we derived from:

$$I_s = |B^{\uparrow\uparrow}.B^{*\downarrow\uparrow}| + |B^{\uparrow\downarrow}.B^{*\downarrow\downarrow}| = \frac{(1-Z)\ Zsin\ \theta}{2.Z\ |Zcos^2(\theta/2) - 1|^2} \ . \tag{3.2}$$

The spin density current I_s at point X, the left interface of FM2, is different from 0. There is no spin density for the exiting wave at point F since only spin up components are present. The net result is a spin density I_s torquing on FM2 as depicted in fig.(3.3) ,the torque created on FM2 is due to the spin accumulation at the left hand side N/FM2 interface.
As suggested by Slonczewski, we phase average the expressions for T and I_s. The phase averaging is justified in a ballistic approach considering that a flux of electrons will show small variations in their Fermi velocities, resulting in small phase differences across the thickness w of the spacer. In fact we average over Z which implies an averaging over phases from 0 to π instead of an expected averaging to 2π. This can be contributed to standing waves being formed within the spacer due to quantum mechanical confinement of the spin down electrons.

The phase averaging of T is done by evaluating the following contour integral over the unity circle C:

$$< T >= \frac{1}{2\pi i} \oint_C T(Z)\ \frac{dZ}{Z} = \frac{1}{2\pi i} \oint_C \frac{-cos^2(\theta/2)(1-Z)^2}{Z^2\ (1 - Zcos^2(\theta/2))(1 - \frac{1}{Z}cos^2(\theta/2)} dZ \ .$$

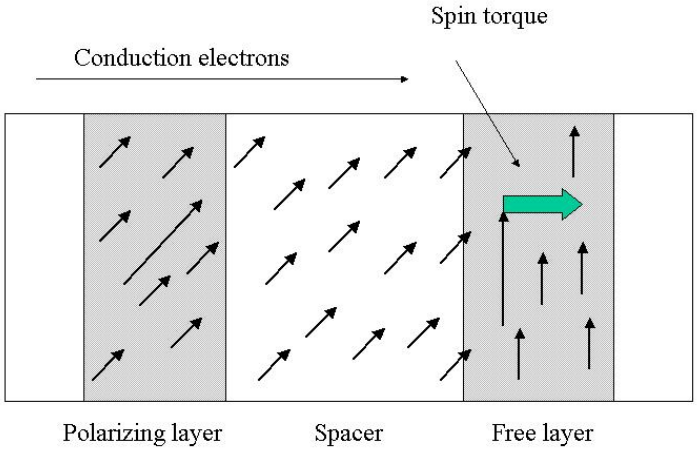

Fig. 3.3 Schematic view of the spin torque. The torque is a result of the transversal component of the spin transfer.

Two poles fall outside the unity circle, and 2 poles $Z_1 = 0$ and $Z_2 = cos^2(\theta/2)$ fall inside the unity circle. Using the residual theorem we obtain:

$$< T >= Res(\frac{T(Z)}{Z}, Z_1) + Res(\frac{T(Z)}{Z}, Z_2) = \sum_i \lim_{Z \to Z_i} (Z - Z_i)\frac{T(Z)}{Z}$$

resulting in

$$< T >= \frac{4\ cos^2(\theta/2)}{(3 + cos\ \theta)}\ . \tag{3.3}$$

Using the same averaging procedure with just one pole $Z_1 = cos^2(\theta/2)$ we also obtain for I_s:

$$< I_s >= \frac{sin\theta}{(3 + cos\ \theta)}\ . \tag{3.4}$$

We now come back to our 3 classes "a", "b", "c" of currents and can write with (3.3) and (3.4) respectively for the total electron and spin density currents:

$$i_e = i_{ea} + i_{eb} + i_{ec} = eJ_a + eJ_b\ \frac{4\ cos^2(\theta/2)}{(3 + cos\ \theta)}\ , \tag{3.5}$$

$$I_s = I_{sa} + I_{sb} + I_{sc} = J_b\ \frac{sin\theta}{(3 + cos\ \theta)}\ . \tag{3.6}$$

Dividing (3.5) by (3.7) we obtain an expression which is depending on J_a/J_b.

$$I_s = \frac{i_e \ sin\theta}{e[-4 + (2 + \frac{J_a}{J_b})(3 + cos\ \theta)]} \ . \tag{3.7}$$

We also demonstrate here that J_a/J_b can be expressed as a function of the polarization factor $P = (n_+ - n_-)/(n_+ - n_-) = (K_+ - K_-)/(K_+ + K_-)$ with n_+, n_- the majority/minority spin densities and K_+, K_- the Fermi wavevectors in the magnets according $V^{\uparrow} = \hbar^2 K_+^2/2m$ and $V^{\downarrow} = \hbar^2 K_-^2/2m$.

We analyze more closely the particle flux densities J_a and J_b. These are electrons injected from a lead from the left hand side of the barrier initially scattering into k-space. Here we have $k_F^2 = k_{\parallel}^2 + k_{\perp}^2$ with k_F the Fermi vector and $k_{\perp}$ and $k_{\parallel}$ respectively the perpendicular and parallel wavevectors. As reference energy we put $E_F = 0$. The spin dependent tunneling is solely determined by $E_{\perp} = -\hbar^2 k_{\perp}^2/2m$ in relationship to the Stoner potentials and considering the zero level Fermi energy. The electrons that will participate in the tunneling process are associated to the 2D density of states given by the disk with radius $k_{\perp}$.

We now reconsider the spin dependent tunneling criteria for the classes "a", "b" and "c" as follows.

Class "a" : $0 \leq k_{\perp} < K_-$: Electrons fully transmit through the double barrier independent of its spin as $E_{\perp} > max\ [V^{\uparrow}, V^{\downarrow}]$.

Class "b" : $K_- < k_{\perp} < K_+$: Only spin up electrons will be transmitted by both magnets. We now have $-K_+^2 < E_{\perp} < -K_-^2$.

Class "c" : $K_- < K_+ < k_{\perp}$: All electrons are blocked since $E_{\perp} < -K_+^2 < -K_-^2$.

We obtain the (uncharged) currents per unit surface from the Landauer-Buttiker formalism taking into account a 2D density of states D(E) from the Fermi disk with radius $k_{\perp}$ and the group velocity $v_{\parallel} = \frac{\hbar}{m}\sqrt{k_F^2 - k_{\perp}^2} = \frac{\hbar}{m}\sqrt{K_+^2 - k_{\perp}^2}$:

$$J = \int_0^{E_{max}} v_{\parallel}.D(E)\ dE = \frac{\hbar}{2\pi m}\int_0^{K_{max}} \sqrt{K_+^2 - k_{\perp}^2}.k_{\perp}\ dk_{\perp} \ . \tag{3.8}$$

Here we follow the Slonczewski ballistic assumption that $k_F = K_+$ so that all spin up electrons will tunnel with T=1. We find respectively for class "a" and "b" the currents :

$$J_a = 2\frac{\hbar}{2\pi m}\int_0^{K_-} \sqrt{K_+^2 - k_{\perp}^2}\, k_{\perp} dk_{\perp} \ , \tag{3.9}$$

$$J_b = \frac{\hbar}{2\pi m}\int_{K_-}^{K_+} \sqrt{K_+^2 - k_{\perp}^2}\, k_{\perp} dk_{\perp} \ . \tag{3.10}$$

Note: In class "a" both spin-up and spin-down are taken into account and in class "b" only spin up.

With the integral identity

$$\int \sqrt{K_+^2 - k_\perp^2}\, k_\perp dk_\perp = \frac{1}{3}\sqrt{K_+^2 - k_\perp^2}.(-K_+^2 + k_\perp^2)$$

we obtain from (9) and (10):

$$2 + \frac{J_a}{J_b} = \frac{2K_+^3}{(K_+^2 - K_-^2)^{3/2}} = \frac{2(2K_+)^3}{8\frac{(K_+ - K_-)^{3/2}}{(K_+ + K_-)^{3/2}}(K_+ + K_-)^3} = \frac{(1+P)^3}{4P^{3/2}} \ . \quad (3.11)$$

Using the relationship between spin current and magnetic moment, $\mu = -\gamma\hbar I_s.A$, and $M = \mu/A.d$ we obtain by identification of (3.11) with (3.7) the reduced expression for the additional spin torque term $\tau(\theta)$ in the LLG equations:

$$\vec{\tau}(\theta) = +\gamma\frac{\hbar.g(\theta)}{e.M_s.A.t.\mu_0}.i.(\vec{m} \times \ \vec{m_p} \times \vec{m}) \ . \quad (3.12)$$

Expressed in SI units with:

$$g(\theta) = \frac{1}{-4 + \frac{(1+P)^3(3+cos\ \theta)}{4P^{3/2}}} \ , \quad (3.13)$$

and e the electron charge, γ the gyromagnetic ratio, M_s the saturation magnetization expressed in A/m, A the surface and d the thickness of the free layer, $i = -i_e.A$ the applied current, $m = |\vec{M}|/M_s$ the reduced magnetization and $\vec{m_p}$ the unity vector to the magnetization of the pinned layer. We used a simplified scattering matrix method not considering any spin flip scattering elements on a basic "ideal" double barrier magnetic structure. However, the same method can be used in full numerical models to calculate spin torques and tunneling probabilities in realistic metallic multilayered structures taking into account several additional interfaces and including spin flip scattering at the interfaces [11].

3.2 FUNDAMENTAL CONSTANTS AND CHARACTERISTIC CURRENT DENSITY

The full LLG equation including the Slonczewski spin torque term is given by

$$\frac{\partial\vec{m}}{\partial t} = -\gamma\vec{m} \times \vec{H_{eff}} + \alpha(\vec{m} \times \frac{\partial\vec{m}}{\partial t}) + \gamma\frac{\hbar.g(\theta)}{eM_sAd\mu_0}.i.(\vec{m} \times \ \vec{m_p} \times \vec{m}) \ . \quad (3.14)$$

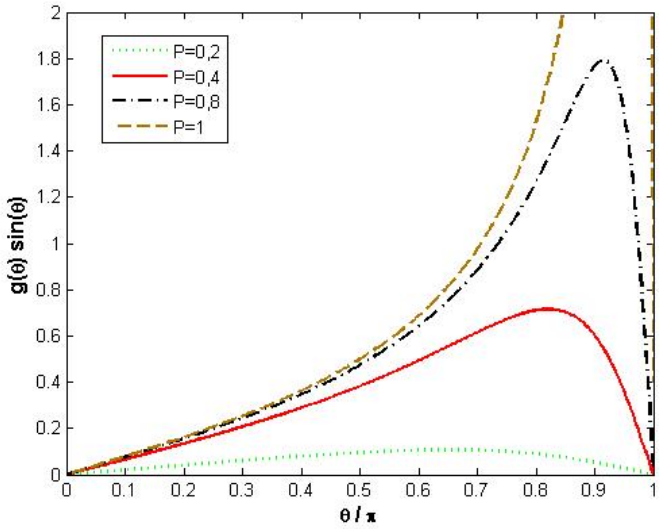

Fig. 3.4 Angle dependent spin torque amplitude for different values of the magnetic polarization P

One of the fundamental constant in the LLG equation is the electron gyromagnetic ratio, expressed in SI units :

$$\gamma_e = \frac{e}{m_e} = \frac{1,6.10^{-19}C}{9.1.10^{-31}kg} = 1.75.10^{11}\ s^{-1}T^{-1}\ . \tag{3.15}$$

We note once again that $\gamma_e.M_s.\mu_0$ has dimensions of frequency as we express M_s in A/m. Therefore we use here and in the previous equations:

$$\gamma = \mu_0.\gamma_e = 2.21\ 10^5\ s^{-1}(A/m)^{-1}\ . \tag{3.16}$$

Typically for the free layer being Cobalt we have:

$$M_s = 1,42.10^6 A/m \rightarrow \gamma M_s = 3,14.10^{11}\ \ s^{-1}\ . \tag{3.17}$$

This means that the time unit in our normalized equation (3.14) corresponds to:

$$\tau = \frac{1}{\gamma M_s} = 3,2\ ps\ . \tag{3.18}$$

Finally we can define a characteristic current density J_p taking into account a typical free layer thickness e.g $d = 2,5$ nm :

$$J_p = \frac{\gamma M_s^2.e.d}{g_e.\mu_B} = 1,15.10^9\ A/cm^2\ . \tag{3.19}$$

This value of current density is a reference to establish if a current is small or big as far as current induced spin torque is concerned. In this respect, it is useful to mention that in most reported experiments in Co-Cu-Co pillars the largest injected current densities are in the order of 10^7 A/cm^2.

3.3 SPIN TRANSFER

Electrons impinging from FM1 will make FM2 to pick up angular spin momentum considering conservation of angular momentum. The change of this angular momentum, called spin transfer, is the sum of inward spin fluxes from both sides of FM2. It can be shown that the average of this spin transfer is proportional to $sin\ \theta$. [9], [1]
The spin transfer effect is mainly an interfacial effect over a typical interface length of 1 nm. Therefore these effects are more important on the thin free layer than on the polarizing thick layer. So the first layer can be considered as a layer with fixed magnetization, where the thin second layer will be influenced by the spin transfer. The role of the spacer is to decouple the ferromagnetic layers. The spacer thickness should be smaller than the spin diffusion length so that the spin polarization gained by the current while crossing the polarizing layer is mostly transmitted to the free layer. When the spin polarized current reaches the interface between the non-magnetic spacer and the second magnetic layer, a perfect spin filtering mechanism occurs. Indeed, a wavefunction for an electron with non-zero spin components can be written as a linear combination of spin up and spin down components. The reflection and transmission probabilities are spin dependent. As a consequence, the reflected and transmitted wave functions differ from each other and from the incident state. This leads to a discontinuity in the transverse spin at the interface.

As a conclusion from above we can consider the origin of the torque as an angular momentum transfer. The angular momentum transfer is the absorption of transverse spin current at the interface. Therefore, to a good approximation the the torque is proportional to the transverse component of the spin current.

4

Macro spin magnetization dynamics with spin transfer torque

In the second chapter we described the LLG equations and the minimization of the micromagnetic energy functional leading to a time-space self consistent solution describing magnetization dynamics. These equations were already known in the early fifties but with the additional spin transfer torque term as described in the third chapter, two new phenomena were predicted. In the second chapter we have shown macrospin solutions of LLG equations. In this chapter we discuss in detail the macrospin magnetization dynamics including the spin transfer torque term. We show as a first new phenomena that the additional Slonczewski term leads to microwave oscillations under certain conditions of injected spin polarized currents and applied external fields. The second phenomena predicted by Slonczewski is full magnetization reversal with or without applied external field. Regardless of the detailed microscopic physics involved we can summarize the equations that govern the spin angular momentum transfer by adding the Slonczewski term to the LLG equations:

$$\frac{\partial \vec{m}}{\partial t} = -\gamma \vec{m} \times \vec{H_{eff}} + \frac{\alpha}{m_s}(\vec{m} \times \frac{\partial \vec{m}}{\partial t}) + \frac{\gamma \hbar J_p}{\mu_0 e d M_s}(\vec{m} \times \vec{m_p} \times \vec{m}) \ , \qquad (4.1)$$

with $\vec{m} = \vec{M}/M_s$ the unit magnetization vector and $\vec{m_p}$ the unit vector parallel to the electron polarization direction. J_p is the current density in A/m^2, M_s the saturation magnetization in A/m and e the electron charge, d is the free layer thickness. For simplicity we also introduce:

$$a_j = \frac{\hbar J_p}{\mu_0 e d} \qquad (4.2)$$

which is proportional to the current density and has dimensions of magnetic field. Experimental verification of the spin torque has been carried out spin valve pillar structures and magnetic tunnel junctions. The spin torque is fundamentally new from the pure precessional term (first term) and from the damping term (second term) in equation (4.1). It is worth mentioning that we have transitioned at this point from previously studied micromagnetics to nanomagnetism, knowing the spin transfer is the result of a quantum spin interference effect. We remark that by solving the LLG equations, the magnetization always moves into lower energy states, eg. the system is looking for an energy minimum. The spin torque neither behaves as an effective field that conserves magnetic energy nor as the damping term which dissipates the energy during motion of magnetization. Simulations in this chapter will demonstrate non conventional effects such as stable precessional states and anomalous hysteresis loops.

4.1 SPIN VALVE GEOMETRY

In order to demonstrate and simulate the new phenomena we mimic an experimental geometry of a spin valve as in fig.(4.1). FM1 is the spin polarizing Co ferromagnet. FM2 is the free magnetic Co layer with typical height of 2,5 nm. In between we have the magnetic insulator NM1 which acts as decoupler of the spin polarizations of FM1 and FM2. This layer is typical made out of Cu of a few nanometers height. The square basis of the spin valve is 64 x 64 nanometers in our numerical model.

We note the additional presence of NM2 and FMref which is a GMR readout unit typically build in into the spin valve. Indeed any magnetization changes of the free layer will cause modulation on the GMR resistance of the full spin valve pillar structure. For completeness we briefly remind the physics behind the GMR effect in the next section. GMR and spin torquing are intimately linked in all applications and experimental set-ups.

4.2 HYSTERESIS LOOPS WITH SPIN TORQUE

The spin valve structure presented in fig. (4.1) is used in OOMMF to simulate hysteresis loops. For Co we use a saturation magnetization M_s of 1,2 T. The uniaxial anisotropy field is 50 mT along the x- axis. No other shape anisotropies (e.g. demagnetizing factors) were taken into account. The external fields are sweeped from -1 T to +4 T. Typical torque currents of 1 to 4 mA are used. In fig. (4.2) we simulate a traditional hysteresis loop without any spin torquing current. Traditional hysteresis loops are calculated by solving the LLG equations for a sweeped external magnetic field. Before each increment of the external field we make sure to have obtained magnetic relaxation by expressing $dM/dt = 0$. We notice that the coercive field of 50 mT is noth-

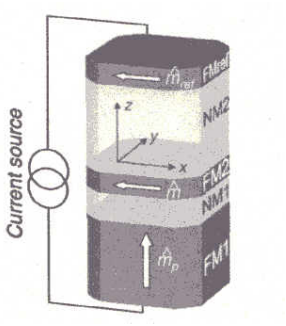

Fig. 4.1 Schematic of a spin valve with a negative spin current defined as the electrons flowing from the thicker to the thinner Co layers. (opposite direction for the current flow).

ing else than the uniaxial anisotropic field. In fig. (4.3) we simulate the same hysteresis loop with a spin torquing current of 1 mA. Unusual oscillations in the hysteresis loop can be observed. The region with rapid variations in m_x correspond to stable precessional oscillations. At those external Zeeman field the magnetization value oscillates. In fig. (4.4) a spin current of 2 mA is applied and the external magnetic Zeeman field is sweeped from -0,5 T to 4 T. Again stable precessions can be noticed and the hysteresis loop changes considerably as seen in fig. (4.3). Additionally, a decreasing magnetization in function of rising external field can be observed in all 3 axes (see also fig. (4.6) which illustrates that the magnetic energy is not always conserved. Another way of illustrating the new phenomena are hysteresis loops where we sweep the applied spin current at fixed external magnetic field along the x-axis. Fig. (4.5) shows another particular phenomena. Aside the zone of stable precessions we notice a zone of stable out of plane magnetization at certain polarized currents -and external field levels. In the next section we analyze this phenomena more in depth.

4.3 CRITICAL CURRENT DENSITIES

In this section we analyze the critical currents necessary to drive magnetization reversal as observed in the previous hysteresis loops. From the technological point of view the challenge is to have as low as possible critical currents. One reason being that high critical current densities are putting high thermal strain on the magnetic and/or semiconductors being used. Another factor is the drive towards lowest power consumption. There is a compromise between low power consumption, fast switching speed and low critical currents. In order to get an insight in these parameters we revert to Eq. (4.1) , (4.2) and

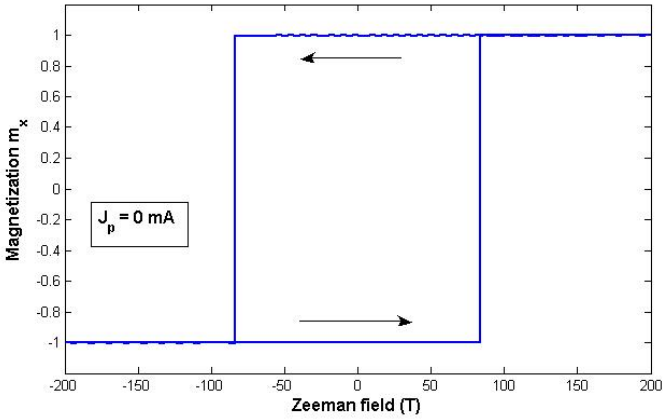

Fig. 4.2 Simulated traditional hysteresis loop without spin torque current obtained by solving the LLG equations for a sweeping external magnetic Zeeman field in the x-direction. As expected the coercive field is equal to the uniaxial anisotropic field.

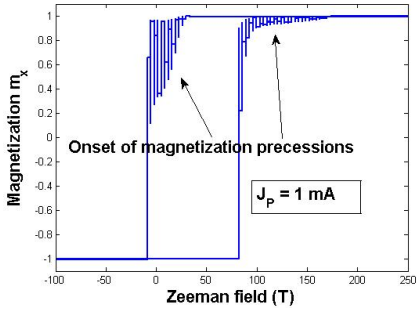

Fig. 4.3 Simulated hysteresis loop with a spin polarized torque current J_p= 1mA. The regions with rapid variations indicate the onset of stable precessional states.

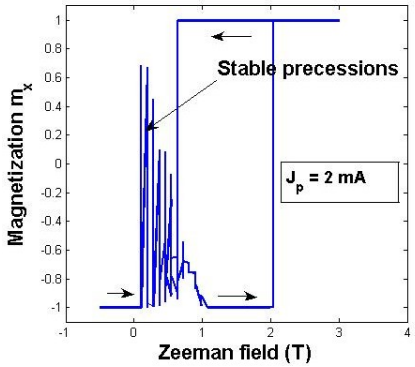

Fig. 4.4 Hysteresis loop with polarized spin torque current J_p= 2mA for a sweeping field between -0,5 T and 3 T in the x-direction. We notice the decreasing magnetization as function of increasing external Zeeman field. This is the result of the spin torque which not necessarily conserves magnetic energy.

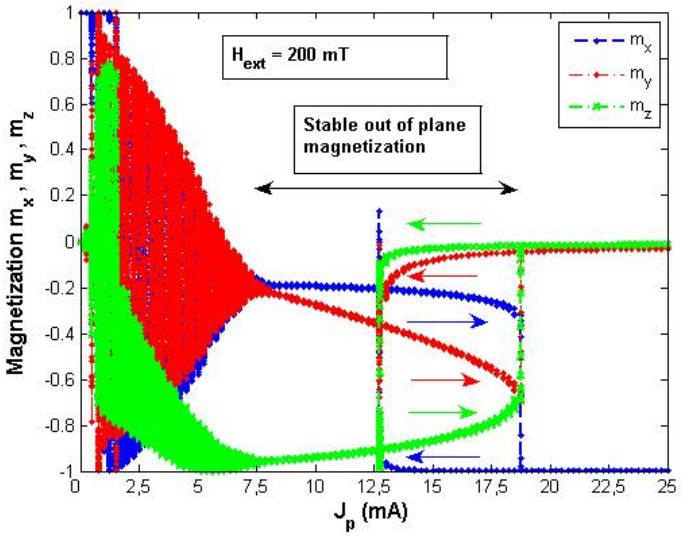

Fig. 4.5 m-J_p simulated hysteresis loop at fixed external Zeeman field of 200 mT and a sweeping spin polarized current J_p from 0 to 25 mA. For $J_p = 7,5mA$ to 18,5 mA we observe non-zero m_y and m_z indicating stable out of plane magnetizations, see fig. (4.6).

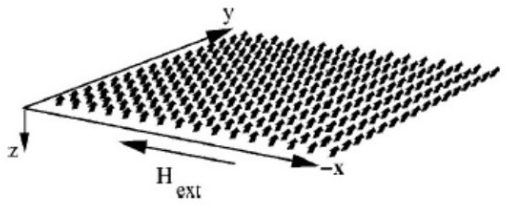

Fig. 4.6 Schematic illustration of a stable out of plane magnetization in a macro-spin configuration.

consider the steady state regime with dM/dt = 0. We use CGS units conform the notations used in [4] and rewrite:

$$\vec{\Gamma} = \vec{M} \times \vec{H_{eff}} - \frac{a_j}{M_s}\vec{M} \times (\vec{M} \times \vec{M_p}) = 0 \ . \tag{4.3}$$

In the case of a uniformly magnetized layer with an anisotropy field along the (1 0 0) axis and an external field along that same axis we can write an analytical expression for H_{eff} with H_K the uniaxial anisotropic field or coercivity:

$$\vec{H_{eff}} = (H_{ext} + H_K M_x/M_s)\vec{e_x} - 4\pi M_z \vec{e_z} \quad with \quad \vec{M_p}//\vec{e_x} \ . \tag{4.4}$$

We calculate the 3 component equations out of Eq. (4.3), (4.4) and after elimination of the M_y component obtain:

$$M_z[(H_{ext} + \frac{H_K M_x}{M_s})^2 + 4\pi M_x(H_{ext} + \frac{H_K M_x}{M_s}) + (\frac{a_j M_x}{M_s})^2] = 0 \ . \tag{4.5}$$

This leads to a trivial solution $M_z = 0$ expressing that the magnetization vector lies at the x-axis or more interesting

$$(H_{ext} + \frac{H_K M_x}{M_s})^2 + 4\pi M_x(H_{ext} + \frac{H_K M_x}{M_s}) + (\frac{a_j M_x}{M_s})^2] = 0 \ . \tag{4.6}$$

Solving for M_x we have:

$$M_x = \frac{-H_{ext}M_s(H_K + 2\pi M_S \pm \sqrt{4\pi^2 {M_s}^2 - a_J^2})}{H_K^2 + 4\pi M_s H_K + a_J^2} \ . \tag{4.7}$$

The components M_y and M_z can be found from the component equations of equation (4.3). For M_z we have :

$$M_z = \pm\sqrt{\frac{(M_s^2 - M_x^2)(-H_{ext}M_s - H_K M_x)}{4\pi M_x M_s}} \ . \tag{4.8}$$

The non zero M_z solutions explain the stable out of plane magnetization. However the equilibrium solutions of Eq. (4.8) are only valid for a finite range of a_j. Another interesting point of Eq. (4.8) is that $dM_x/dH_{ext} < 0$, which explains the specific shape noticed in the hysteresis loops. The last interesting feature is that there is a critical current density above which the spin torque can be used to switch the magnetic configuration from eg. parallel to anti-parallel. If uniform magnetization is assumed the critical currents can be easily derived from Eq. (4.1) taking into account the $M = \pm M_s e_x$:

$$(a_j)_{crit} = \pm\alpha(2\pi M_s + H_K) + \alpha H_{ext} \ . \tag{4.9}$$

4.4 STABLE MAGNETIC PRECESSIONAL STATES

In previous hysteresis loops we noticed already stable precessional states. In this section we zoom in on the trajectories of these precessional states. In fig. (4.7) we see an example of such a trajectory. After a transition phase the precession becomes permanent. The magnetization oscillates with a stable frequency. Needless to say that the industry is looking for novel kinds of spintronic oscillators using this effect. These Spin Torque Oscillators (STO) seem to have very stable frequencies when cascades of several spin valves are being used. In fig. (4.7) we have simulated the frequencies by simple Fast Fourier Transform of the oscillations seen in fig. (4.7). The spectrum shown in fig. (4.8) indicates that no frequency-current linearity exists. Furthermore there is an onset of 1/f noise for increasing spin torque currents that are of real concern for possible electronic applications. Typical frequencies being sustained are within the X-band microwave region. Research on STO's are focused in understanding and eliminating the 1/f noise by choosing different damping parameters and or by playing with different magnetic layers and interfaces within the build up of the spin valves. Up to date the onset of this noise is not yet fully understood and various theories are being explored.

Fig. (4.9) illustrates a typical fully calculated phase diagram [12] as normalized magnetoresistance $\Delta R/R$ with varying currents and fields.

4.5 PULSE INDUCED MAGNETIZATION REVERSAL - MRAM

In fig. (4.10) we show a full magnetization reversal induced by a subnanosecond 1,6 mA spin polarized current injection. This effect as anticipated by Slonczewski lies at the basis of novel memory devices called SMT-MRAM (Spin Momentum Transfer - Magnetoresistive Random Access Memory). It is interesting to mention that such a magnetization reversal can happen at zero external magnetic field. SMT-MRAM devices have potentially high speed read/write cycles and lower power consumption than older MRAM writing schemes. It is anticipated that full industrial scale up of SMT-MRAM will

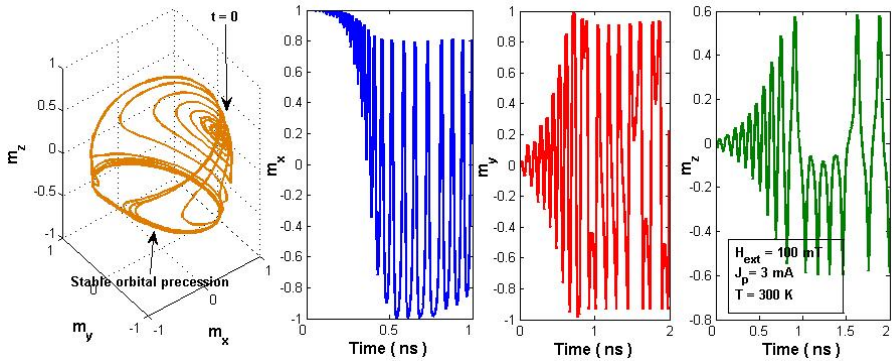

Fig. 4.7 Trajectory of stable precessional state with $J_p = 3mA$, $H_{ext} = 100mT$ and alpha damping = 0,3. We notice the initial transition phase and entrance into the stable precession after more then 2 ns. Sampling time is 50 ps in order to visualize the transition magnetization. Once the stable orbit achieved, some jitter is noticed due to continuing precessional forces. This jitter can result in noise when analyzing the spectrum.

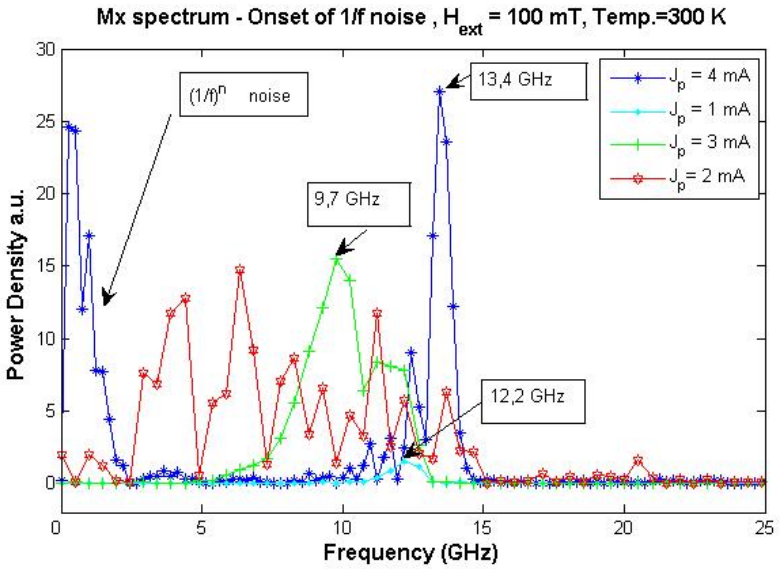

Fig. 4.8 Spin torque oscillator frequency spectrum. Onset of 1/f noise arises at currents above 2 mA.

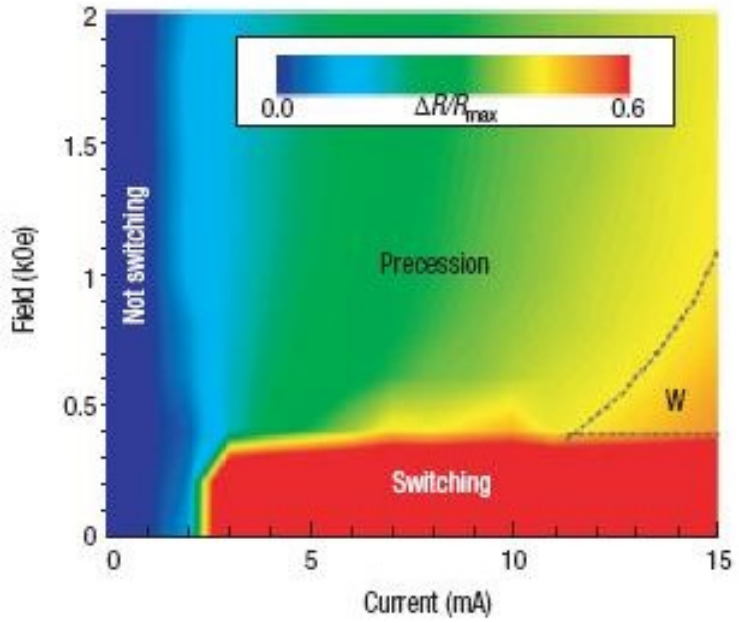

Fig. 4.9 Fully calculated phase diagram from [12] as normalized magnetoresistance with varying currents and fields. Three area's can be distinguished including full magnetization reversal (switching), non switching zone and phase coherent precession. Zone "W" indicates non coherent precessions of the magnetic domain inducing noise.

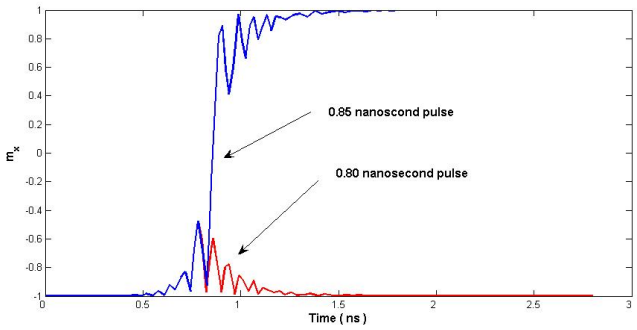

Fig. 4.10 Macrospin MRAM effect by injection of a subnanosecond spin polarized current. A 0.8 ns pulse does not result in full magnetization reversal, a 0.85 ns pulse triggers full reversal.

revolutionize current memory devices with faster access and longer lifetimes than flash, its main competitor. Hard drives in computer could potentially be replaced by novel non volatile SMT-MRAM's in the coming years resulting in very fast powering up of computers and eventually replacing traditional hard disks.

4.6 ENERGY DISSIPATION AND ENERGY PUMPING

In this section we study the variation of the magnetic energy of the system. In the classical LLG equations the change of magnetic energy can be easily derived as :

$$\frac{dE}{dt} = -\frac{\alpha\gamma}{1+\alpha^2}\frac{1}{M_s}|\vec{H_{eff}} \times \vec{M}|^2 \ . \tag{4.10}$$

It can be seen that $dE/dt < 0$. This means that any non parallel configuration will continuously dissipate energy until the magnetic energy reaches its local minimum with $H_{eff}//M$. However when the spin torque term becomes active the loss of energy can be compensated by the additional spin torque energy term :

$$\frac{dE}{dt} = -\frac{\gamma}{1+\alpha^2}\frac{1}{M_s}[\alpha|\vec{H_{eff}} \times \vec{M}|^2 - \alpha_j(|\alpha M_s \vec{M_p} - \vec{M} \times \vec{M_p}) \times (\vec{H_{eff}} \times \vec{M})|] \ . \tag{4.11}$$

The first term in Eq. (4.11) is the energy loss due to damping and the second term is due to energy in- or output due to spin torque. If the first term is less than the second then $dE/dt > 0$, the magnetic energy will increase. If the first and second term are exactly balanced the net energy term loss is

zero and therefore stable out of plane magnetization states are possible while $|\vec{M} \times \vec{H_{eff}}| \neq 0$ but $d\vec{M}/dt = 0$.

4.7 STOCHASTIC LANGEVIN TEMPERATURE DYNAMICS : IMPACT ON THE SWITCHING TIME

In this section we simulate the thermally activated magnetic fluctuations. The thermal activation is modeled with a random magnetic field that is superimposed to the effective magnetic field after each time iteration and is localized on each cell. The field magnitude follows a Gaussian distribution with its variance given by the fluctuation-dissipation theorem [7]:

$$< \vec{H}_i(t_1).\vec{H}_j(t_2) >= \mu\delta_{ij}\delta(t_1 - t_2) \ , \tag{4.12}$$

where:

$$\mu = \frac{2k_B T\alpha}{V_{cell} M_s \gamma \Delta t} \ , \tag{4.13}$$

and k_B the Boltzmann constant, $\Delta t = 10\ ps$ is chosen so that the simulation results are insensitive to any further decreasing of Δt. V_{cell}= 64 nm x 64 nm x 2,5 nm in our case. An additional module in OOMMF allows for full temperature simulations. Fig. (4.11) and (4.12) illustrate the impact of the Langevin dynamics on magnetization reversal at zero external field. It is important to mention that we have not performed full statistical analysis of the switching impact due to temperature. We have just shown that the full Langevin-LLG-Slonczewski equations can be solved within the OOMMF framework and that temperature effects need to be taken into account in advanced nano-magnetic simulations.

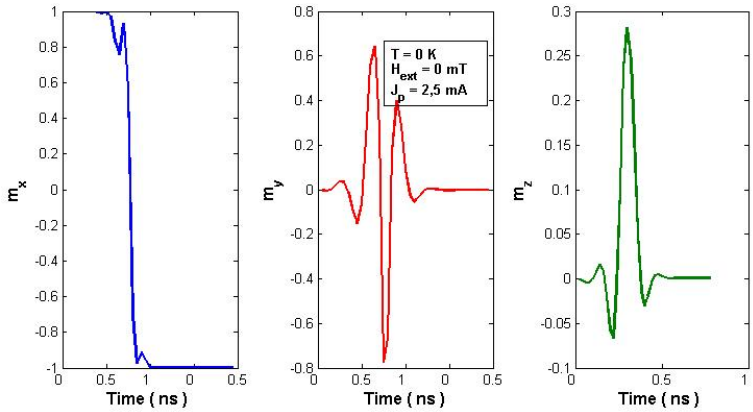

Fig. 4.11 Simulated switching time at 0 K including the Langevin dynamics. Typical magnetization reversal time is 0,5 ns at zero external field and a 2,5 mA spin torque current.

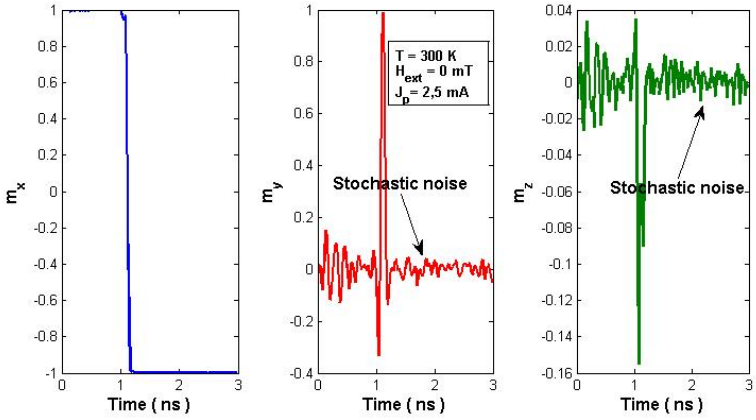

Fig. 4.12 Simulated switching time at 300 K solving the full Langevin-LLG-Slonczewski equations. The stochastical noise due to the increased temperature becomes visible. Switching time is affected and does increase to 1 ns.

5

Full domain nano-magnetic modeling

In the previous chapter we have gained substantial insight in the spin torque effects leading to stable precessions, stable out of plane magnetization or full magnetization reversal. However the macrospin model has serious limitations as no full degaussing can be applied. In this chapter we study full domain simulations including non-uniform demagnetizing fields in realistic geometries as derived in chapter two, Eq. (2.27). In the following simulations we use a Co magnetic film in our Co/Cu/Co spin valve with typical exchange constant $A = 20.10^{-12}$ J/m, $M_s = 1,4.10^6$ A/m, polarizing factor P=0,5669 and $\alpha = 0,014$.

5.1 EXCITATIONS OF INCOHERENT SPIN WAVES

In the macrospin model, within the switching region we have seen coherent precession modes that under certain spin torque currents lead to full magnetization reversal (SMT-MRAM effect). In the study of full magnetic domains more complex dynamics are observed but stable domain precessions and full magnetic reversal remain valid. In fig. (5.1) we simulate full magnetization reversal on a typical ellipse shaped domain with dimensions 129 x 72 x 3 nm. Before switching, three consecutive stages showing quite different magnetization motions can be noticed. In the first stage we see the growth of precessional amplitudes followed by a second stage of coherent precessions. In the third stage incoherent precessions arise just before the full magnetization reversal. The exact role of the coherent precessions are still unexplained however one

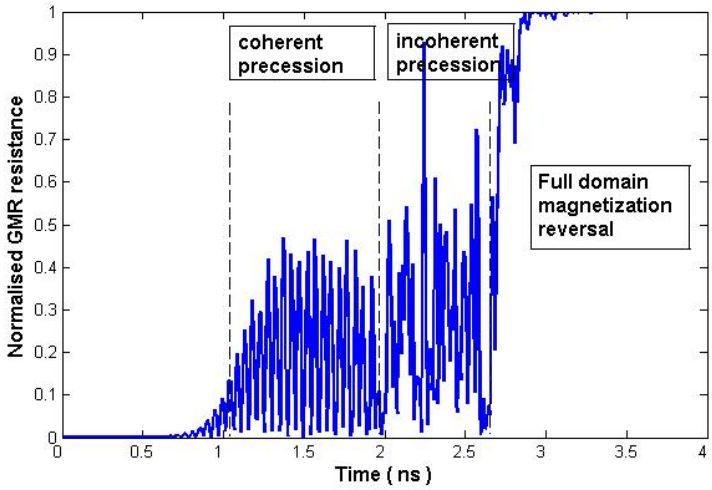

Fig. 5.1 Normalized GMR switching as function of time for a spin current of 5 mA and zero external field. The GMR value has been calculated by averaging the magnetization along the main ellipse axis m_x. At the onset of the spin torque current small precessions start in the first phase. Gradually coherent precessions appear in the second phase. In the last stage incoherent precessions are observed just before full magnetization reversal.

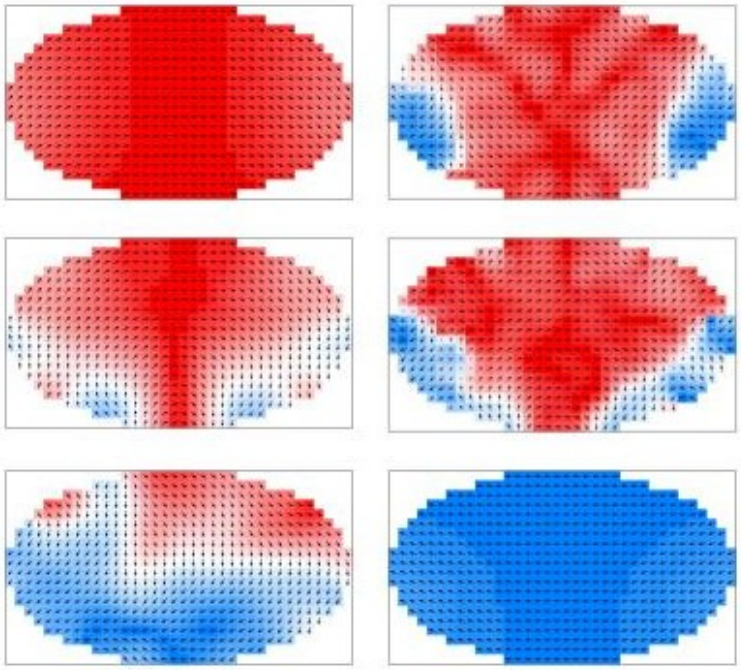

Fig. 5.2 Magnetization switching dynamics for a spin current of 5mA and zero external field. Red color is anti-parallel magnetization and blue color parallel magnetization in the xy-plane. Top left: initial precessions starting at domain extremities. Top right: after 0.8 ns. Middle left: 1,4 ns. Middle right: 2,1 ns. Lower left : 2,6 ns. Lower right: full magnetization reversal after 3 ns.

can assume that the incoherent precessions play an important role in the full magnetization reversal of the domain. It is important to mention that the incoherent precessions will generate broad spectral noise causing unwanted noise propagation in potential computer applications. In fig. (5.7) we show typical magnetization dynamics preceding the full magnetization reversal. We refer to the support CD, spin1.wmv, for the full motion simulation.

In fig. (5.3) we show typical sustained incoherent precessions for a 14 mA spin current at an external field of 600 Oe. Fig. (5.3) shows the corresponding energy evolution of the system. We note that these precessions are within the W-zone as mentioned in fig. (4.9).

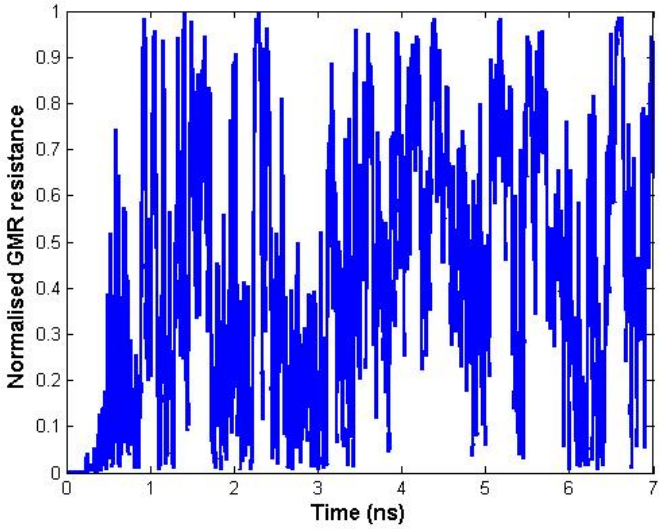

Fig. 5.3 Sustained incoherent domain precessions expressed in normalized GMR resistance in the case of a 14 mA spin current and 600 Oe external field.

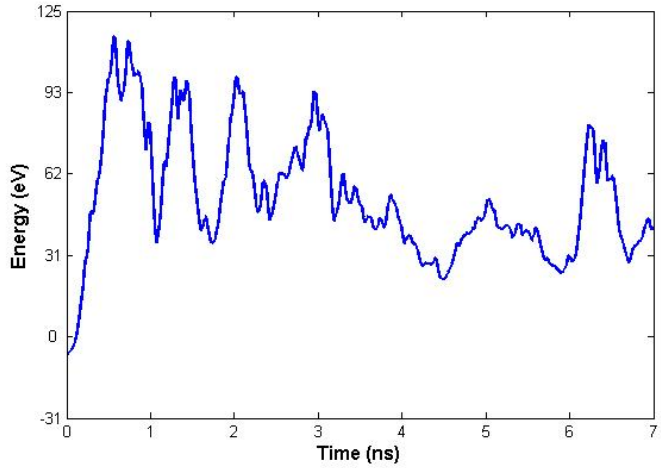

Fig. 5.4 Energy time evolution showing sustained incoherent precessions in the case of 14 mA spin current and 600 Oe external field.

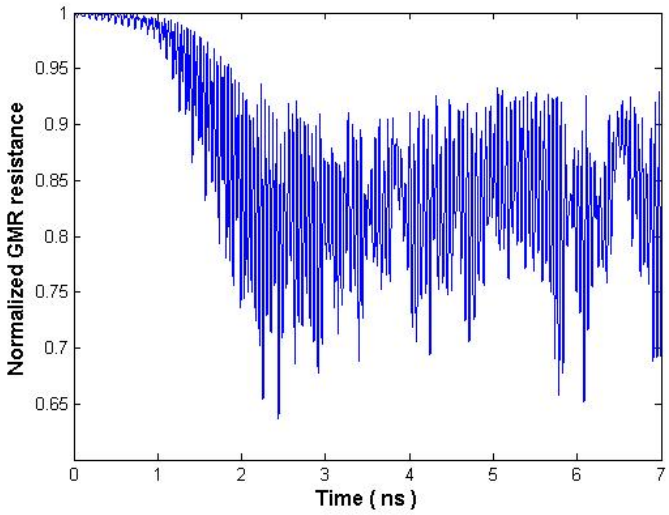

Fig. 5.5 Sustained coherent domain precessions expressed in normalized GMR resistance in the case of 4 mA spin current and 1 kOe external field.

5.2 EXCITATIONS OF COHERENT SPIN WAVES

Referring to the phase diagram of fig. (4.9) we simulate in fig. (5.5) coherent spin waves with a 4 mA current and an external field of 1 kOe. We refer to the support CD, spin2.wmv, for the full motion simulation. These domain magnetizations are at the base for the development of novel microwave spin torque oscillators.

5.3 IMPACT OF CONTACT POINT SPIN CURRENT INJECTION ON THE MAGNETIZATION DYNAMICS

As mentioned in chapter 4, coherent domain precessions can be used in the manufacturing of novel spin torque oscillators (STO). As shown in fig. (4.8) and in our various simulations, magnetic dynamics by spin currents in nanopillars can be chaotic over a wide range of currents and external fields leading to a broadening of linewidth or even 1/f noise in the spectrum. Recently, microwave spectra with sharp peaks have been observed in point contact experiments. In these experiments, because of the point contact geometry, the physical edges of the samples are far from the excited region. As a result, the effective field is more homogeneous over the excited region so that the magnetic excitations can develop in a more uniform way, eventually leading to a

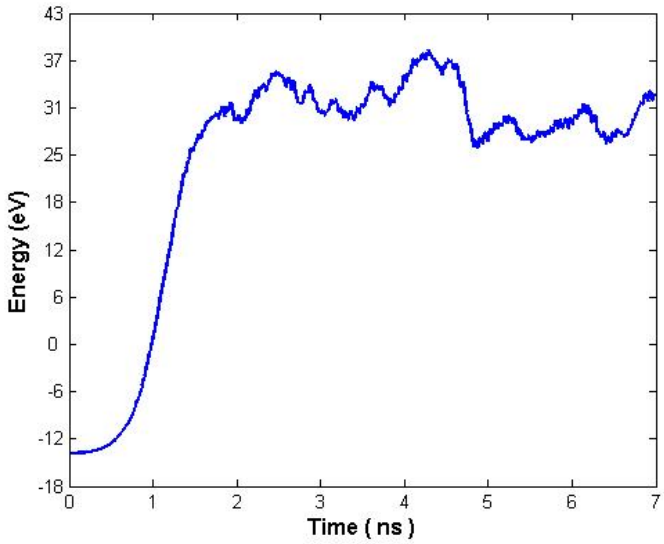

Fig. 5.6 Energy time evolution showing coherent precessions in case of 4 mA spin current and 1 kOe external field.

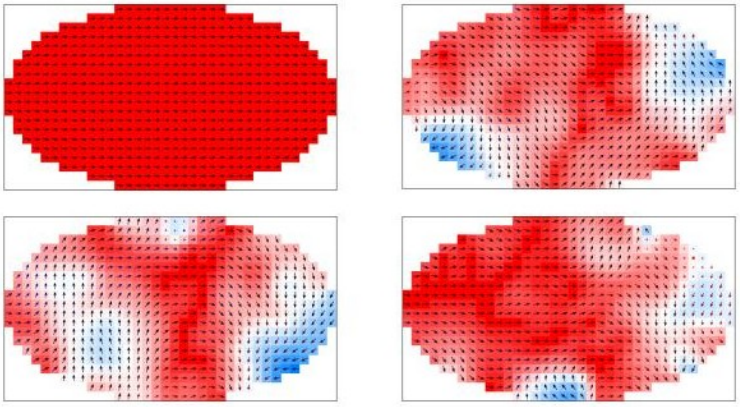

Fig. 5.7 Sustained coherent precession magnetization dynamics. Red color is anti-parallel magnetization and blue color parallel magnetization in the xy-plane. Top left: initial precessions starting at domain extremities. Top right: after 2.3 ns. Lower left : after 4.4 ns. Lower right: after 6.7 ns.

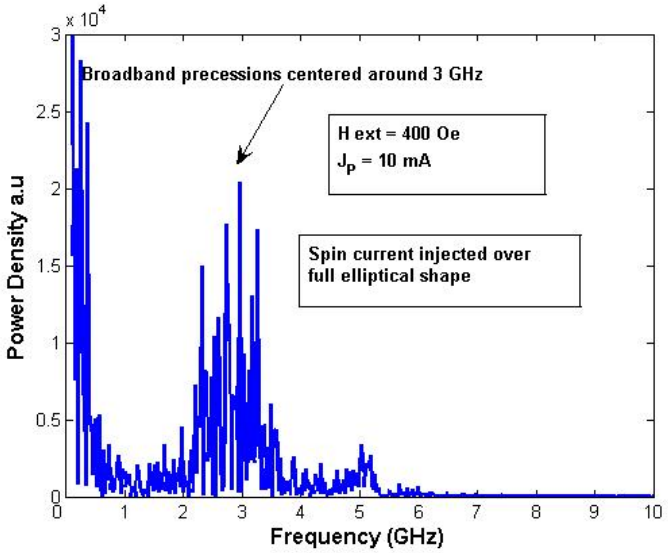

Fig. 5.8 Spin current injected over full elliptical shape. Broadband 3 Ghz spectrum at 10 mA and 400 Oe.

more coherent precession of the magnetization, [10], [21], [22]. In fig. (5.8), (5.9), (5.10) , (5.11) we simulate the effect of respective full current flow over the entire elliptical surface or contact point current flow over a circular point contact with 50 nm radius centered in the middle of the elliptical surface. We conclude that there is a substantial impact for point contact current injections going from chaotic oscillations to full magnetization reversal or from no effect at all to stable oscillations. However we must mention that we have not been able to simulate pure spectral peak narrowing or the elimination of spurious signals in the spectrum. Further simulations are probably necessary with other types of point contacts to confirm these recent experimental observations.

5.4 MRAM - STATE OF THE ART

As it became clear in 2003 that MRAM was a viable universal memory [25], several manufacturers started industrial scale production in various wafer technologies. Fig. (5.12) shows prototype MRAM chips from Freescale, Honeywell, Motorola and IBM. It is important to mention that this MRAM technology is currently not based on spin torque switching but rather on external bit/word lines generating magnetic switching fields, see fig. (5.13). However, these devices have high power consumptions which increases further upon

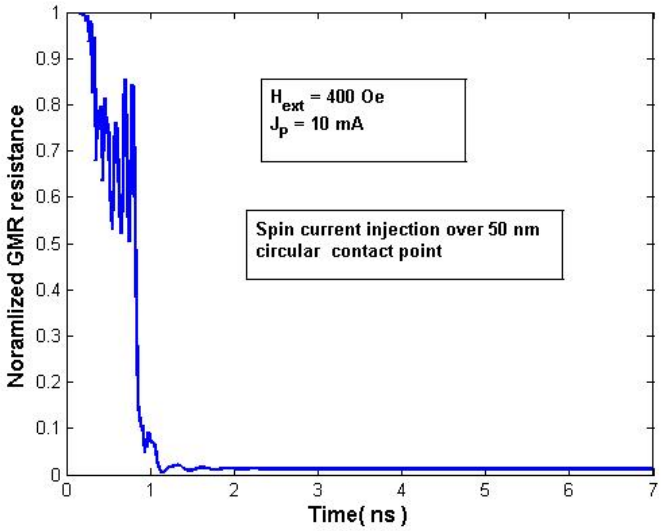

Fig. 5.9 Spin current injection over 50 nm contact point. Same conditions as in fig. (5.8). Instead of stable precessions full magnetization reversal is obtained.

lowering the bit size due to the inverse dependence of the switching field on length scales. For SMT-MRAM the power consumption scales down quadratically with length scales since the critical current density is important. On the longer term and for smaller size elements, we can see other limitations such as thermal effects (paragraph 4.7) and noise contributions which will dominate over the spin torque currents. Since a non-scalable memory technology is not commercially viable, we conclude that the technological realization of SMT-MRAM is the deciding factor weather MRAM will overhaul the memory market on short term or not. A lot of worldwide research is geared towards that objective.

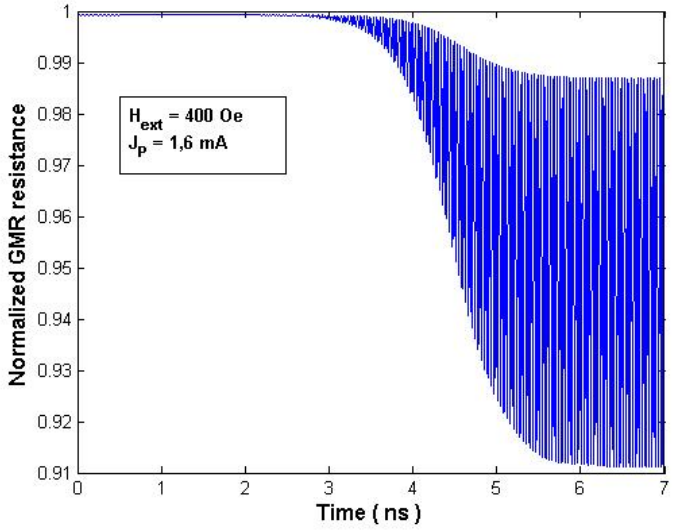

Fig. 5.10 Weak coherent magnetization precessions at 1,6 mA and 400 Oe with 50 nm contact point current injection. With full elliptical current injection no precessions at all would be observed. Motion dynamics to be viewed with spin3.wmv on the support CD.

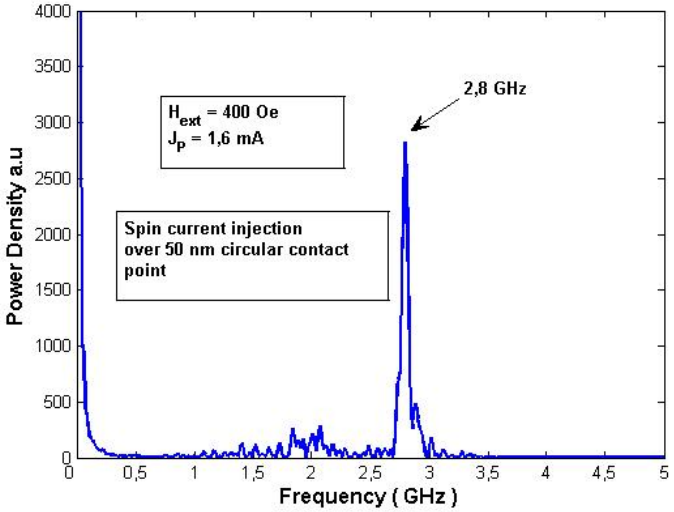

Fig. 5.11 Spectrum related to fig. (5.10).

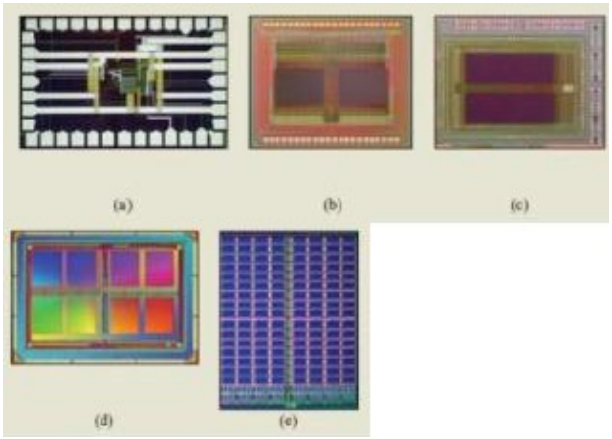

Fig. 5.12 Photomicrographs showing the increasing density of prototype MRAM chips. a) IBM 1 mm x 1,5 mm 1 kB chip in 0,25 μ technology with 3-10 ns access time. b) Motorola 3,9 mm x 3,2 mm 256 kB in 0,6 μ technology with 35 ns access time. c) Motorola 4,25 mm x 5,89 mm 1 Mb chip in 0,6 μ technology with 50 ns access time. d) Freescale 4,5 mm x 6,3 mm 4 Mb chip in 180 nm technology with 25 ns access time. e) IBM 7,9 mm x 10 mm 16 Mb chip in 180 nm technology with 30 ns access time. Picture from [25].

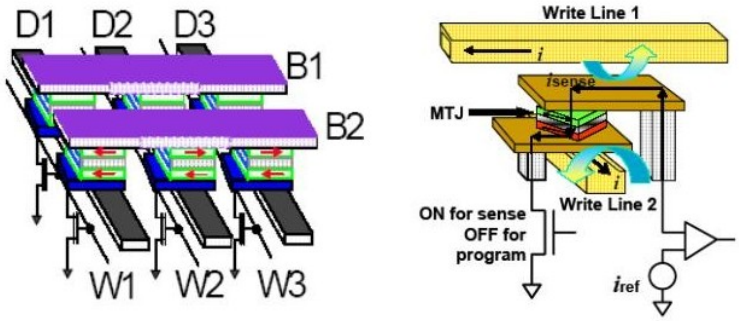

Fig. 5.13 Freescale MRAM concept with bit and word lines generating magnetic switching fields. The read-out is done over the GMR effect within the MTJ. The high power requirements still make this an intermediary step before turning to full spin torque MRAM. (Freescale Research and Development)

6

Spin pumping and enhanced Gilbert damping

A final contribution to the torque on the free layer comes from a phenomena called "spin pumping". The switching characteristics of a magnetic system depends essentially on the Gilbert damping constant α. In the previous chapters we have kept α nearly constant around 0,014 for Co. We have also seen that α governs the technological important critical currents and magnetization reversal time of the ferromagnetic layer. Typical intrinsic values for transition metal ferromagnets are smaller than $\alpha_0 < 10^{-2}$. This value is smaller than its optimum value of $\alpha > 10^{-1}$ for fast switching. The mechanism of spin pumping and enhanced Gilbert damping as described in this chapter, if well controlled, allows for the engineering of the Gilbert damping constant to optimize the high speed magneto-electronic devices. Gilbert damping constants can be experimentally studied in thin film ferromagnetic films by measuring ferromagnetic resonance (FMR) line-widths. In general these experiments indicate that α is in some cases to be found quite large in comparison with its bulk value α_0. Furthermore it seems that α sensitively depends on the substrate and capping layer materials used. For example with a 20 $\AA$-thick permalloy (Py) film sandwiched between two Pt layers, the damping constant is found to be 10^{-1}, while in the bulk state the value is 10^{-2}. In the following sections we will give a basic explanation for the observed discrepancies. We limit ourselves to an overview of the formalism of the adiabatic spin-pump theory. We refer to [23] for the full derivation based on a scattering-matrix approach to formulate a circuit theory for the spin pumping phenomena. The circuit theory makes use of transmission and reflection matrices, r_{mn} and t_{mn} as derived in chapter 3, leading to a conductance matrix $g^{\uparrow\downarrow}$ with spin states

σ:

$$g^{\sigma\sigma'} = \Sigma_{mn}[\delta_{mn} - r^{\sigma}_{mn}(r^{\sigma'}_{mn})^*] \ , \tag{6.1}$$

where m and n label the transverse modes at the Fermi level in a normal metal film. In the next section we also introduce the complex spin conductance matrix A.

6.1 PRECESSION-INDUCED SPIN PUMPING

Since a spin polarized current incident from a non-magnet can produce magnetization dynamics in adjacent ferromagnet, it is not unreasonable to suggest that the motion of the magnetization of a ferromagnet can influence the spin current in an adjacent non-magnet. The most prominent effect is the injection of a spin current into the non-magnet whenever the magnetization moves. One consequence of the injected spin current is a back-reaction torque that increases the damping of the spin motion. These effects have been confirmed by experiments. We consider a sandwich structure N-F-N as shown in fig. (6.1). The circuit theory makes use of transmission and reflection matrices, r_{mn} and t_{mn} as derived in chapter 3, leading to a conductance matrix $g^{\uparrow\downarrow}$ with spin states σ:

$$g^{\sigma\sigma'} = \Sigma_{mn}[\delta_{mn} - r^{\sigma}_{mn}(r^{\sigma'}_{mn})^*] \ , \tag{6.2}$$

where m and n label the transverse modes at the Fermi level in a normal metal film. Without any voltage bias, no spin or charge currents flow when the magnetization of the ferromagnet F is constant in time. If the situation changes e.g. under the influence of an external magnetic field and the magnetization direction starts precessing, a spin current is pumped out of the ferromagnet. The current pumped into the N layer depends on a complex value $A = A_r + A_i$ called the spin pumping conductance. I_s^{pump} can be written as [23]:

$$I_s^{pump} = \frac{\hbar}{4\pi}(A_r m \times \frac{dm}{dt} - A_i \frac{dm}{dt}). \tag{6.3}$$

The spin conductance matrix is related to the conductance matrix by:

$$A = g^{\uparrow\downarrow} - t^{\uparrow\downarrow} \ . \tag{6.4}$$

The spin pumping will also cause a spin accumulation μ_s. Assuming an adiabatic system, we have $I_s^{pump} = I_s^{back}$. From magneto-electronic circuit theory one can derive for I_s^{back}:

$$I_s^{back} = \frac{1}{2\pi}(g_r^{\uparrow\downarrow}\mu_s + g_i^{\uparrow\downarrow} m \times \mu_s) \tag{6.5}$$

$$= \frac{\hbar}{4\pi}(g_r^{\uparrow\downarrow} m \times \frac{dm}{dt} - g_i^{\uparrow\downarrow}\frac{dm}{dt}) \ . \tag{6.6}$$

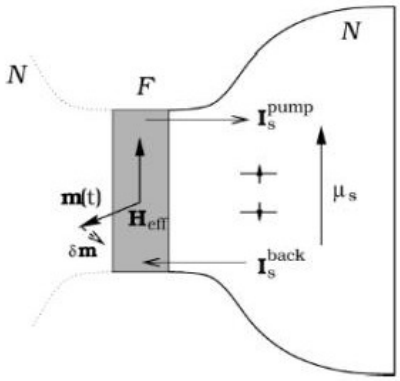

Fig. 6.1 Ferromagnetic film F sandwiched between two non magnetic reservoirs N. We consider only the right reservoir and assume the left fully insulating. The spin pumping current I_s^{pump} and the spin accumulation μ_s in the right reservoir can be found by applying circuit theory to the steady state $I_s^{pump} = I^{back}$, [23].

The contribution to I_s due to the spin accumulation driven current becomes:

$$I_s = I_s^{pump} - I_s^{back} \ . \tag{6.7}$$

If the normal metal layer represents a perfect spin sink, then all spins injected into the normal metal layer relax by spin-flip processes or leave the system. In that case we have $I_s^{pump} \simeq I_s^{back}$ and $I_s \simeq 0$. With $I_s \simeq 0$ no back spin current exists and no back torque is expected. However, in the case of a non perfect spin sink and in a steady state regime, $I_s \neq 0$. Indeed, I_s^{pump} and I_s^{back} can take different values. It can be easily shown that the energy associated with the Larmor frequency of the magnetization precession, results in the same splitting between the chemical potentials $\mu^{\uparrow}$ and $\mu^{\downarrow}$, see fig. (6.2). The spin current out of the ferromagnet carries angular momentum perpendicular to the magnetization direction. By conservation of angular momentum, the spins ejected by I_s correspond to a torque $\tau = -I_s$ on the ferromagnet. If possible interfacial processes are neglected, the torque τ is fully transmitted to the magnetization precession. We obtain finally an additional spin torque term and can rewrite the LLG equations as:

$$\frac{\partial \vec{m}}{\partial t} = -\gamma \vec{m} \times \vec{H_{eff}} + \alpha_0 \cdot (\vec{m} \times \frac{\partial \vec{m}}{\partial t}) + \frac{\gamma}{M_s V}.I_s \ , \tag{6.8}$$

where α_0 is the dimensionless Gilbert damping constant. The intrinsic bulk constant α_0 is smaller than the total damping $\alpha = \alpha_0 + \alpha'$. The additional damping α' caused by the spin pumping is observable in FMR experiments. For completeness we refer to [24] for the derivation of an angle dependence of

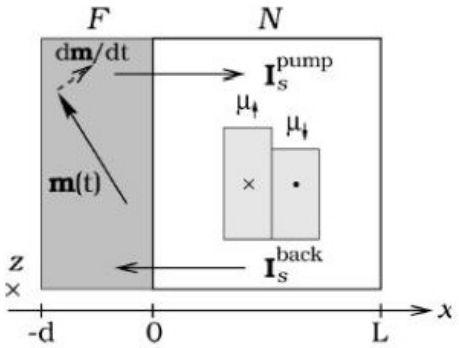

Fig. 6.2 The spin-up and spin-down chemical potentials are split by $\mu_s = \hbar\omega$, the energy of the corresponding Larmor frequency of the original precessional perturbation. When the ferromagnetic magnetization steadily rotates around the $z - axis$, $m \times \dot{m}$ and the normal-metal spin accumulation $\mu_s(x)$ are oriented along z. In contrast with fig. (6.1) we consider here a non perfect spin pump resulting in $I_s \neq 0$, [23], [24].

the enhanced Gilbert damping α':

$$\frac{\alpha'(\theta)}{\alpha'(0)} = 1 - \frac{\nu sin^2\theta}{1 - \nu^2 cos^2\theta} \ , \tag{6.9}$$

where $\alpha'(0) = \gamma\hbar g_r^{\uparrow\downarrow}/8\pi M_s dS$. For small angle $\theta \approx 0$ we have:

$$\frac{\alpha'(\theta)}{\alpha'(0)} \approx \frac{1}{1 + s(1 - cos\theta)} \ , \tag{6.10}$$

where $s = \nu/(1 - \nu)$.
For Co/Cu spin valves we have $g^{\uparrow\downarrow}/S = 2,94.10^{19}\ m^{-2}$ and $\nu = 0,98$ for Cu.

7

Circuit theory of spin transfer torques in symmetric and asymmetric spin valves.

7.1 SYMMETRIC SPIN VALVES

There is still disagreement between experiment and theory that describe spin transfer in spin valves. In the previous chapters we have used the sine transfer model which is widely used in the literature. It is basically geometry independent as the $g(\theta)$ term is kept constant. The only remaining term is the sine term in Eq. (3.14). As we have assumed in chapter 3, there is no spin dependent scattering at the free-layer interface as majority or minority carriers either fully transmit or reflect at the interfaces and the polarization of the current that flows from the fixed to the free layer is independent of the free layer orientation. However, Slonczewski has published another important paper in 2002, [2], taking into account spin dependent reflections at the fixed-layer interface. In this paper Slonczewski developed a spin transfer torque theory that combines a density matrix description of the spacer with a circuit theory description of the remainder of the structure. He worked out the algebra for the case where the spacer layer is thin and the spin valve is symmetric (identical ferromagnets and leads), and found the torque L_s to be the same on the left and right spacer/ferromagnet interfaces,

$$L_S(\theta) = \frac{\hbar I}{2e} \frac{P\Lambda^2 sin\theta}{(\Lambda^2+1)+(\Lambda^2-1)cos\theta} \ , \tag{7.1}$$

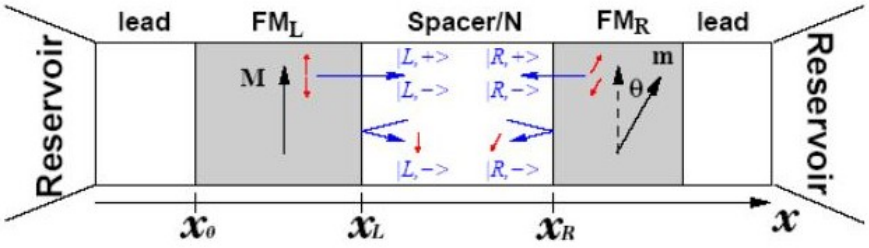

Fig. 7.1 Asymmetric five layer spin valve. A nonmagnetic spacer layer separates two ferromagnetic layers whose magnetization are inclined from another by an angle θ. A nonmagnetic lead connects each ferromagnet to an electron reservoir, from [15].

In this formula, I is the total current that flows through the structure,

$$P = \frac{\frac{1}{2}(R_\downarrow - R_\uparrow)}{\frac{1}{2}(R_\downarrow + R_\uparrow)} = \frac{r}{R} \; and \;\; \Lambda^2 = GR \; . \tag{7.2}$$

$R_\uparrow$ and $R_\downarrow$ are effective resistances experienced by spin-up and spin-down electrons between the reservoirs and the spacer layer, with $G = Se^2k_F^2/4\pi^2\hbar$ the conductance with k_F the Fermi wave vector and S the device cross section surface. This is called the symmetric Slonczewski SS approximation.

7.2 ASYMMETRIC SPIN VALVES

For some asymmetric geometries, fig. (7.1), a previously unsuspected feature of the torque leads to the prediction of stable precessions that does not occur for the symmetric case. The electric current in a real physical spin valve can be written as the sum of spatially varying currents carried by up and down electrons: $I = I_\uparrow(x) + I_\downarrow(x)$. The corresponding spin current is $\Delta I(x) = I_\uparrow(x) - I_\downarrow(x)$. The up and down spin voltage (chemical potential) drops along the spin valve are $V_\uparrow(x)$ and $V_\downarrow(x)$. Slonczewski related the function $I_\uparrow(x)$ to the values $I_\uparrow^L = I_\uparrow(x_L)$ and $I_\uparrow^R = I_\uparrow(x_R)$ and similarly for $I_\downarrow(x)$. He also writes $\Delta V_R = V_\uparrow(x_R) - V_\downarrow(x_R)$ for the up-down difference in the voltage drop from the right reservoir to a point in the spacer infinitesimally close to the interface between the spacer and the right ferromagnet. ΔV_L is defined similarly.
With this model, Slonczewski wrote down (but did not completely solve) all the equations needed for the asymmetric geometry. Two of the linear equations relate the voltage drop differences to the spin currents,

$$0 = \Delta V_L(1+cos^2\theta) - G^{-1}\Delta I_L sin^2\theta - 2\Delta V_R cos\theta \ , \quad (7.3)$$
$$0 = \Delta I_L(1+cos^2\theta) - G\Delta_L sin^2\theta - 2\Delta I_R cos\theta \ . \quad (7.4)$$

Two additional equations describe the voltage drop differences in terms of effective resistances R_L, R_R, r_L and r_R.

$$\Delta V_L = \Delta I_L R_L + I r_L \ , \quad (7.5)$$
$$\Delta V_R = \Delta I_R R_R + I r_R \ . \quad (7.6)$$

Finally Slonczewski derived expressions for the interfacial torques. At respectively $x = x_R$ and $x = x_R$ the torques are:

$$L_R = \frac{\hbar}{2e}\frac{\Delta I_R cos\theta - \Delta I_L}{sin\theta} \ , \quad (7.7)$$
$$L_L = \frac{\hbar}{2e}\frac{\Delta I_L cos\theta - \Delta I_R}{sin\theta} \ . \quad (7.8)$$

It is now simple to solve the previous four equations for the unknowns, ΔI_L, ΔI_R, ΔV_L and ΔV_R. We obtain:

$$L_R = \frac{\hbar}{2e} I sin\theta [\frac{q_+}{A + Bcos\theta} + \frac{q_-}{A - Bcos\theta}] \ , \quad (7.9)$$

where,

$$q_\pm = \frac{1}{2}[P_L\Lambda_L^2\sqrt{\frac{\lambda_R^2+1}{\lambda_L^2+1}} \pm P_R\Lambda_R^2\sqrt{\frac{\lambda_L^2-1}{\lambda_L^2-1}}] \ , \quad (7.10)$$
$$A = \sqrt{(\Lambda_L^2+1)(\Lambda_R^2+1)} \ , \quad (7.11)$$
$$B = \sqrt{(\Lambda_L^2-1)(\Lambda_R^2-1)} \ . \quad (7.12)$$

The parameters P_L, P_R, Λ_L, and Λ_R are defined in terms of R_L, R_R, r_L and r_R as P and Λ are defined in Eq. (7.2) in terms of R and r. For the symmetric case we have $\Lambda_L = \Lambda_R = \Lambda$ and $P_L = P_R = P$. This makes $q_- = 0$ and we fall back into the symmetric case as described in Eq. (7.1). It can be shown [26] that the term in q_- can qualitatively influence the magnetization dynamics.

7.3 ASYMMETRIC VERSUS SYMMETRIC SPIN VALVES

In fig. (7.2) we show the differences between a symmetric and asymmetric spin valve. We consider a spin valve with film thicknesses Cu(10nm)/Co(40nm)/Cu(thin)/Co(3nm)/Cu(180) nm which is very asymmetric. The Cu/Co bilayers on opposite sides of the spacer layer are very different. The left bilayer is mostly ferromagnet, the right bilayer is mostly non-magnetic. The difference in Slonczewski terms for the symmetric and asymmetric torques in this geometry is still small as depicted in fig. (7.2), nevertheless it is large enough to produce small in plane precessions, [15].

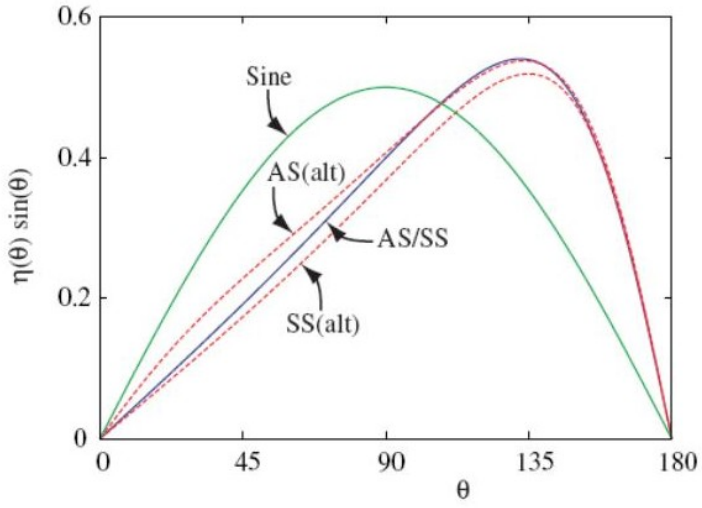

Fig. 7.2 Various forms of spin transfer torque as a function of the angle θ between the fixed and free layer. The sine torque does not depend on the spin valve geometry. The symmetric and asymmetric Slonczewski torques are identical for certain geometries but are different for the geometry which was discussed in this chapter (dashed lines), from [15].

8

Conclusion

We conclude that any major progress in theoretical spintronics necessarily implies a better understanding of the microscopic theory of spin dependent electrical quantum transport. Whether one calculates a Tunneling Magneto Resistance in a GMR device or derives a spin transfer torque, the main questions remain about which spin interactions to consider. As examples of this controversy we refer to chapter 3 were we derived the sine transfer torque term in detail. We have considered diagonal terms in the scattering matrices with full transmission or reflection for majority or minority carriers. The off-diagonal terms were zero implying no scattering effects at the interfaces between the non magnetic and magnetic free layer. This model works well and is widely accepted in the literature. However in chapter 7 we summarized the symmetric and asymmetric spin torque terms derived from a density matrix approach taking into account interface scattering and formalized by circuit theory. For certain geometries of spin valves only few differences are noticed. Various other variations of spin transfer torque terms exist in the literature. Unfortunately it is difficult to put forward a coherent picture from all these various approaches as the authors make different assumptions about the spin transfer effects they believe are important when describing the magnetization dynamics. There is generally no consensus today about which spin transfer torque model will prevail, however the experimentalist strive to a minimal model that puts LLG simulations in line with experimental results. From a computational point of view we believe that the scattering matrix method is convenient as it allows to easily model multiple stacked layers once the scattering matrices that characterize the layers are known. This is even more valid as we have been able to fully reproduce the torque term and its amplitude-angle

dependency $g(\theta)$ of Slonczewski's original paper using this method, including the phase averaging as suggested by him. In our approach we have been inspired by [11]. Probably the choice of the spin torque term will ultimately be determined experimentally through a material characterization.

We have noticed in chapter 5, while reproducing the results published in [12], that magnetization reversal goes hand in hand with phases of coherent precessions followed by incoherent precessions just before magnetization reversal. On the one hand incoherent precessions play an important role in the reversal mechanism but on the other hand it generates noise that we want to avoid in spintronic applications. The origin of this noise mechanism is not yet well understood. More modeling is required playing with different additional interfaces, capping materials and or different damping constants to compromise between noise and switching performance. Therefore engineered enhanced damping parameters based on the spin pumping concept summarized in chapter 6 could become important. However, only few publications are available on spin pumping theory, [23], [24].

Finally, we conclude about the technological applications. It is generally acknowledged that SMT-MRAM has the potential in overhauling the complete memory chip market. It is currently retained as the most important driving factor behind the industrial scaling of spin transfer technology.

8.1 MOST IMPORTANT REALIZATIONS DURING THIS THESIS

1. Literature overview of phenomenological and microscopic theories: LLG, spin transfer, spin torque, spin pumping and spin accumulation.
2. Alternative derivation of Slonczewski's original sine spin transfer term using a scattering matrix method.
3. Mastering a novel, nano-magnetic modeling tool for solving 2D LLG equations including spin torquing. (OOMMF software from NIST)
4. Simulation of most important magnetization dynamics such as full magnetization reversal and stable precessions in macro-spin and full magnetic domain. Simulation of Langevin and 1/f noise. Study of the impact of contact point spin injection.
5. Discussion of some of the critical factors in technological applications such as SMT-MRAM and STO.

9

Dutch Summary

9.1 INLEIDING TOT DE SPINTRONICA

Onze traditionele elektronica is op zuivere ladingstransfer gebaseerd en houdt geen rekening met de spin van de elektronen tijdens het elektrisch transport. De huidige halfgeleider industrie is sinds de uitvinding van de transistor door W. Shockley, J. Bardeen en W. Brattain op deze opvattingen gebaseerd. In de spintronica doet de spin van het elektron, zoals omschreven door de wetten van de kwantummechanica, voor het eerst zijn intrede. Men zal in de beschrijving van het elektrisch transport een strikt onderscheid moeten maken tussen 'spin-up' en 'spin-down' gepolariseerde elektronen. De injektie van zulk een spin gepolariseerde stroom in een magnetisch gelaagde struktuur geeft aanleiding tot een volledig nieuwe en intrigerende fysica. Verdere ontwikkelingen van de spintronica hebben het potentieel om onze halfgeleider industrie in de komende decennia fundamenteel te veranderen.

In de jaren '50 hebben Landau en Lifschitz reeds micromagnetische studies uitgevoerd aan de hand van de naar hen genaamde Landau-Lifschitz-Gilbert vergelijkingen. Deze vergelijkingen vormen tot heden de basis van de magnetica en worden o.a. gebruikt in de engineering van magnetische materialen. In 1988 hebben A. Fert en M.N. Baibich het Giant Magneto Resistance (GMR) effekt ondekt, waarbij een modulatie van de weerstand van een gelaagde magnetische struktuur werd vastgesteld in funktie van een extern aanwezig magnetisch veld. Dit effekt is zuiver te verklaren aan de hand van spin afhankelijk transport waarbij de verstrooiingseigenschappen spin afhankelijk zijn. Principieel heeft dit te maken met verschillende toestandsdichtheden van het fer-

romagnetisch materiaal naargelang de 'spin-up' of 'spin down' toestand van het elektron. Algemeen wordt deze ontdekking aanzien als het begin van de spintronica. GMR heeft op zich ongekend snelle technologische toepassingen gekend in de computer industrie, o.a. in de leeskoppen van harde schijven. Tien jaar later, in 1996, heeft J.C. Slonczewski van IBM de spintronica een tweede impuls gegeven door het effekt te beschrijven van een aktieve spin gepolariseerde stroom doorheen zulk een GMR struktuur. Twee belangrijke theoretische fenomenen werden voorspeld nl. de volledig spin torque geinduceerde magnetische omkering en stabiele magnetische precessies. Er wordt verwacht dat het koppelen van deze nieuwe fysische fenomenen aan nieuwe magnetisch gedopeerde halfgeleiders de basis zal vormen van de volgende generatie nano-elektronische componenten.

9.2 GILBERT DEMPING EN RUIS IN MAGNETISCH GELAAGDE GMR STRUKTUREN

In deze thesis geven we naast een beknopt overzicht van GMR een gedetailleerd overzicht en alternatieve afleiding van de originele berekeningen van J.C. Slonczewski. Een scattering matrix methode wordt gebruikt om de effekten van de spin transfer en spin accumulatie in een gelaagde magnetische struktuur te berekenen. Deze methode is naar onze opvattingen eenvoudiger dan de origineel gebruikte WKB methode van Slonczewski. In het derde hoofdstuk simuleren we numeriek de belangrijkste nieuwe fysische fenomenen. Hiervoor maken we gebruik van een door NIST ontwikkelde software, OOMMF, die voor het eerst ook de volledige LLG-Slonczewski vergelijkingen oplost voor willekeurige magnetische gelaagde stukturen. We vinden in macrospin simulaties zowel de stabiele magnetische precessies als de volledige magnetische omkering terug. We tonen aan dat het mogelijk is om via Langevin dynamica thermische stochastiche ruis aan de LLG Slonczewski vergelijkingen toe te voegen en aldus ook temperatuurseffekten in rekening te brengen. In hoofdstuk 5 herhalen we deze simulaties voor twee-dimensionele gelaagde strukturen door het in rekening brengen van de degaussing velden. Hierbij wordt aandacht besteed aan inherente ruiseigenschappen en fase coherentie problemen tijdens het magneto-dynamisch process. De spin torque geinduceerde magnetische omkering koestert hoge verwachtingen in random access memory chip toepassingen (MRAM). De stabiele magnetische precessies kunnen gebruikt worden in nieuwe nanotechnologische oscillatoren. Belangrijk is om op te merken dat deze spin transfer theorie enkel in magnetische lagen met nanodimensies tot uiting komt gezien dat de spindiffusie lengte kleiner moet zijn dan de gebruikte magnetische laagdiktes. Zoals dikwijls in de fysica hebben simultane technologische evoluties in het maken van nanostrukturen het mogelijk gemaakt om deze nieuwe spin transfer theorie ook in de praktijk te kunnen omzetten. In hoofdstuk 6 besteden we aandacht aan nieuwe fenome-

nen zoals 'spin pumping' en 'verhoogde Gilbert demping'. De nanostrukturen hebben inderdaad tot gevolg dat de intrinsieke bulk materiaal eigenschappen in de nano-dimensies andere waarden aannemen dan we gewoon zijn. In het laatste hoofdstuk bespreken we kort de laatste ontwikkelingen op het gebied van de equivalente netwerktheorie voor de omschrijving van de spin transfer effekten. Deze theorie wordt hedendaags het meest in de praktijk gebruikt. Tenslotte willen wij vermelden dat de spin transfer theorie zoals voorspeld door Slonczewski pas in 2006 voor het eerst technologisch gedemonstreerd kon worden in een zeer select aantal onderzoeksinstellingen. Dit maakt het onderzoek in het kader van deze thesis bijzonder aantrekkelijk en motiverend.

Martin Keller

10

Support CD

In annex we provide a CD containing the most important tools and results of this thesis.

- OOMMF
  Contains the latest OOMMF (Object Oriented Micromagnetic Framework) software version 1.2.a.4. To this date this is still a non officially released beta version. It is the first OOMMF version including Slonczewsky spin torquing.
  This software is pre-compiled and can be readily used.
  It contains in its subfolders an extensive documentation file. The library contains sample MIF files of various applications in TCL/TK language of which some have been used during this work.
  We refer also to http://math.nist.gov/oommf/ for further information.
  With special thanks to dr. M. Donahue and dr. D. Porter from NIST for making this beta version available and for their kind e-mail support during the various implementations of the add-on's such as the Langevin module.

- Movies, magnetic domain dimensions are 129 x 72 x 3 nm.
  Spin1.wmv and Spin4.wmv
  Shows the SMT-MRAM effect. Full domain magnetic reversal sequence with zero external magnetic field and respective spin currents of 5 mA and 10 mA.
  Spin2.wmv
  Sustained incoherent precessions with spin current of 4 mA and external field of 1 kOe.

Spin3.wmv
Weak coherent precessions with 1,6 mA spin current over a contact point of 50 nm and a 400 Oe external field.

- Publication
  Folder contains most relevant publications consulted during the realization of this thesis.

- Thesis
  Contains .tex and .pdf files of this thesis including all graphical support

- Simulation results
  Contains some .odt simulation results as generated by the mmGraph module. These files can be read into Matlab via the "uiimport" function. .omf files can be converted to .gif files within the OOMMF shell via the DOS command "tclsh oommf.tcl avf2ppm -ipat *.omf -opatsub .gif -format B24 ppmtogif". Movies have been generated with Windows Media Player.

References

1. J.C. Slonczewski, *Current driven excitation of magnetic multilayers*, Journal of Magnetism and Magnetic Materials, 159, L1-L7, (1996).

2. J.C. Slonczewski, *Currents and torques in metallic magnetic multilayers*, Journal of Magnetism and Magnetic Materials, 247, 324-338, (2002).

3. A.D. Kent , B. Ozyilmaz, E.del. Barco, *Spin-transfer-induced precessional magnetization reversal*, Applied Physics Letters, 84, 3897, (2004).

4. Z. Li, S. Zhang, *Magnetization dynamics with a spin-transfer torque*, Physical Review B, 68, 024404, (2003).

5. P.M. Braganca, I.N. Krivorotov, O. Ozatay, A.G.F. Garcia, N.C. Emley, J.C. Sankey, D.C. Ralph, R.A. Buhrman, *Reducing the critical current for short-pulse spin-transfer switching of nanomagnets*, Applied Physics letter, 87, 112507, (2005).

6. J.G. Zhu, *Spin transfer induced noise in CPP read heads*, IEEE transactions on magnets, 40, 182, (2004).

7. J.G. Zhu, *Thermal magnetic noise and spectra in spin valve heads*, Appl. Phys., 91, 7273, (2002).

8. E.Y. Tsymbal, D.G. Pettifor, *Perspectives of Giant Magnetoresistance*, Solid State Physics Ed. H. Ehrenreich and F. Spaepen, vol. 56, 113-237, Academic Press 2001.

9. L. Berger, *Emission of spin waves by a magnetic multilayer traversed by a current*, Physical Review B, 54, 9353, (1996).

10. W.H. Rippard, M.R Pufall, S. Kaka, S.E Russek, T.J Silva, *Direct-current induced dynamics in $Co_{90}Fe_{10}/Ni_{80}Fe_{20}$ point contacts*, Phys. Rev. Lett. 92, 027201, (2004).

11. X. Waintal, E. Myers, P.W.Brouwer, and D.C Ralph, *Role of spin-dependent interface scattering in generating current-induced torques in magnetic multilayers*, Physical Review B, 62, 12317, (2000).

12. K.J. Lee, A. Deac, O. Redon, J.P Nozières, B. Dieny, *Excitations of incoherent spin-waves due to spin-transfer torque*, Nature Materials, 3, 877, (2004).

13. A. Maria Deac, *Spin-transfer effects in spin valves for CPP-GMR heads: A static and dynamic investigation*, Phd thesis June 2005, Joseph Fourier University - Grenoble.

14. M. D'Aquino, *Nonlinear Magnetization dynamics in thin films and nanoparticles*, Phd thesis December 2004, University of Napels "Frederico II".

15. J. Xiao, *Spin-Transfer Torque in Magnetic Nanostructures*, Phd thesis August 2006, School of Physics, Georgia Institute of Technology.

16. M. Donahue and D. Porter, *Object Oriented Micromagnetic Framework - Programming Manual*, November 18th, 2005, NIST - USA. Website: http://math.nist.gov/oommf

17. M. Abramowitz and I. Stegun, *Handbook of mathematical functions* (Dover, New York, 1970).

18. A. Hubert and R. Schäfer, *Magnetic domains, The analysis of Magnetic Microstructures* (Springer, 1998)

19. O. Heinonen, *Computational applied magnetics* (Seagate Technology, july 2003), website: http://www.seagate.com

20. P. Krstajić, *Magnetism and tunneling in diluted magnetic semiconductors structures*, Phd thesis, Universiteit Antwerpen, 2006.

21. J.V. Kim and C. Chappert, *Stochastic theory of spin-transfer oscillator*, Phys. Rev. B 73, 174412, (2006).

22. Q. Mistral, Joo-Von Kim, T. Devolder, P. Crozat, C. Chappert, J. A. Katine, M.J. Careyand and K. Ito, *Current-driven microwave oscillations in current perpendicular-to-plane spin-valve nanopillar*, Appl. Phys. Lett., 88, 192507, (2006).

23. Y. Tserkovnyak, A. Brataas, G.E. Bauer, *Spin pumping and magnetization dynamics in metallic multilayers*, Physical Review, B 66, 224403, (2002).

24. Y. Tserkovnyak, A. Brataas, G.E. Bauer and B.I. Halperin, *Nonlocal magnetization dynamics in ferromagnetic hybrid nanostructures*, Rev. Mod. Phys, 77, 1375, (2005).

25. S.A. Wolf, A.Y. Chtchelkanova, D.M. Treger, *Spintronics - A retrospective and perspective*, IBM J. Res. and Dev., vol.50, No.1, (2006).

26. J. Xiao, A. Zangwill, M.D. Stiles, *Boltzmann test of Slonczewski's theory of spin-transfer torque*, Physical Review, B 70, 172405, (2004).